Dynamics and wall collision of inertial particles in a solid-liquid turbulent channel flow

MASOUD EBRAHIMIAN[1], R. SEAN SANDERS[2], SINA GHAEMI[1,†]

[1]Department of Mechanical Engineering, University of Alberta, Edmonton, Alberta, Canada
[2]Department of Chemical and Materials Engineering, University of Alberta, Edmonton, Alberta, Canada

The dynamics and wall collision of inertial particles were investigated in non-isotropic turbulence of a horizontal liquid channel flow. The inertial particles were 125 µm glass beads at a volumetric concentration of 0.03%. The bead-laden flow and the unladen base case had the same volumetric flow rates, with a shear Reynolds number (Re_τ) of the unladen flow equal to 410 based on the half channel height and friction velocity. Lagrangian measurements of three-dimensional trajectories of both fluid tracers and glass beads were obtained using time-resolved particle tracking velocimetry based on shake-the-box algorithm of Schanz et al. (*Exp. in Fluids*, vol. 57, no. 5, 2016, page: 1-27). The analysis showed that on average the near-wall glass beads decelerate in the streamwise direction, while farther away from the wall, the streamwise acceleration of glass beads became positive. The ejection motions provided a local maximum streamwise acceleration above the buffer layer by transporting glass beads to high velocity layers and exposing them to a high drag force in the streamwise direction. Conversely, the sweep motion made the maximum contribution to the average streamwise deceleration of glass beads in the near-wall region. The wall-normal acceleration of beads was positive in the vicinity of the wall, and it became negative farther from the wall. The investigation showed that the glass beads with sweeping motion had the maximum momentum, streamwise deceleration, and wall-normal acceleration among all the beads close to the wall and these values increased with increasing their trajectory angle. The investigation of the beads that collided with the wall showed that those with shallow impact angles (less than 1.5º) typically slide along the wall. The sliding beads had a small streamwise momentum exchange of ~5% during these events. The duration of their sliding motion could be as much as five times the inner time scale of the unladen flow. The wall-normal velocity of these beads after sliding was greater than their wall-normal velocity before sliding, and was associated with the rotation induced lift force. Beads with impact angles greater than 1.5º had shorter interaction times with the wall and smaller streamwise and wall-normal restitution ratios.

Key words: turbulent particle-laden flow, Lagrangian particle tracking velocimetry, particle acceleration, particle-wall collision

1. Introduction

The time-dependent motion of a small spherical particle in a non-uniform Stokes flow can be described by the Maxey-Riley equation (Maxey & Riley 1983). Since 1983, a few studies have been conducted to extend the application of this equation to unsteady flows (Mei & Adrian, 1992) and larger Reynolds number (Kim et al. 1998). However, the equation is still limited to the motion of a single sphere in a low *Re* flow. Moreover, the Saffman (due to pressure distribution on the particle) and Magnus (due to particle rotation) lift forces, which are known to be important for large particles in turbulent flow have not been included in these equations (Crowe et al. 2012; Kim and Balachandar 2012; Meller & Liberzon 2015). These forces along with the wall repulsive force (Brenner 1961; Feng et al. 1994), particle-particle, and particle-wall collisions affect particle dynamics in turbulent particle-laden flow (Crowe et al. 2012). Therefore, to better model inertial particle motion in turbulent flows and support the continued development of numerical approaches, high-quality experimental data of particle dynamics for such flows are required. The latter can be obtained by measurement of particle acceleration through Lagrangian particle tracking techniques.

One of the first measurements of acceleration of inertial particles in a turbulent boundary layer was conducted by Gerashchenko et al. (2008). They recorded the two-dimensional trajectories of small (sub-Kolmogorov scale)

† Email address for correspondence: ghaemi@ualberta.ca

air-borne water droplets. The Stokes number (St, the ratio of particle relaxation time to the flow time scale) of the droplets based on the Kolmogorov time-scale (t_K) was in the range of $0.035 \leq St_K \leq 1.2$ at a small mass loading of 0.01%. The droplets close to the wall were characterized as having an average streamwise deceleration ($\langle A_x \rangle < 0$, where A_x is the instantaneous streamwise acceleration and $\langle\ \rangle$ is the ensemble average operator). Similar results were also obtained from numerical studies of turbulent particle-laden flows by Lavezzo et al. (2010), Zamansky et al. (2011), and Yu et al. (2016). These investigations used DNS for the fluid phase along with simplified versions of the Maxey-Riley equation for the solid phase. The numerical simulation of Lavezzo et al. (2010) was carried out for $0.87 \leq St_K \leq 11.8$, Zamansky et al. (2011) for $1 \leq St^+ \leq 25$ (where St^+ is defined based on the inner time-scale of the flow), and Yu et al. (2016) at $St^+ = 35$. Each of these studies reported $\langle A_x \rangle < 0$ in the near-wall region and related it to the dominant effect of viscous force on the particles. There is, however, a discrepancy in the values of the average wall-normal acceleration, $\langle A_y \rangle$, as discussed below.

In the experiments of Gerashchenko et al. (2008), the droplets had $\langle A_y \rangle < 0$, with the positive axis pointing away from the wall. These droplets were sub-Kolmogorov, and had a high density ratio with respect to the carrier phase (~833). Also, droplets do not rebound when they hit the wall, which is not the case for solid particles. The numerical simulations of Lavezzo et al. (2010) and Yu et al. (2016) also resulted in $\langle A_y \rangle < 0$ for both unladen and particle-laden flows in the near-wall region while the Zamansky et al. (2011) simulations showed that $\langle A_y \rangle > 0$. All these numerical simulations assumed point-wise particles and neglected pressure distribution on the particle, near-wall lift, added-mass, and Basset forces. These forces are important when the particles are larger than the smallest scale of the flow (Calzavarini et al. 2012). The aforementioned numerical studies also assumed elastic particle-wall interaction, and neglected wall repulsive force, and particle-particle collisions. Further development of the numerical simulations of turbulent particle-laden flows requires investigation of the effects of particle-related forces on their dynamics through collection and evaluation of experimental data.

The relationship between St and particle acceleration has been previously investigated in turbulent flows to understand particle dynamics. The investigations have shown the remarkable effect of St on the probability density function (pdf) and root-mean-square (rms) of particle acceleration (a). For example, Ayyalasomayajula et al. (2006) analyzed the effect of St_K on the acceleration distribution of droplets in grid turbulence, which is isotropic. It was found that increasing St_K from 0.09 to 0.15 narrowed the pdf of A_x and made its rms (i.e. a_x) smaller. This trend was also reported by Bec et al. (2006) who used DNS to investigate the effect of St_K on pdf and rms of particles acceleration with $St_K < 3.5$ in isotropic turbulent flows. The narrower tails of the acceleration pdf and its smaller a at higher St_K in isotropic turbulence have been related to the effect of particle inertia on its motion; inertial particles are less responsive to the fluid motion and more likely to move out of vortices (where there are high acceleration motions) to regions with higher strain (Eaton & Fessler 1994; Ayyalasomayajula et al. 2006; Gerashchenko et al. 2008; Lavezzo et al. 2010).

In non-isotropic turbulence as would occur near a wall, a different relationship between St_K and a_x has been reported. For example, in the experimental study mentioned earlier, Gerashchenko et al. (2008) showed that increasing St_K from 0.07 to 0.47 increased a_x and suggested that this trend was because of the effect of gravity and mean shear on inertial particles. Lavezzo et al. (2010) conducted a DNS of particle-laden flow with and without gravity in non-isotropic turbulence to verify the effect of gravity on the relationship between St_K and a_x. The parameters of their simulation, including the particle/fluid density ratio and St_K, were similar to those studied by Gerashchenko et al. (2008). In the study of Lavezzo et al. (2010), particles were able to collide with the wall and elastically rebound from it, in contrast to the droplets in the experiment of Gerashchenko et al. (2008). The comparison of the simulations of Lavezzo et al. (2010) with and without gravity confirmed that the increase in a_x with increasing St_K close to the wall is due to the combined effects of gravity and mean shear. They argued that the downward motion of the particles due to gravity exposes them to a strong deceleration due to the mean shear very close to the wall and causes high a_x. The analysis of Lavezzo et al. (2010) showed that with increasing St_K from 0.87 to 1.76, the a_x slightly increased even in the absence of gravity (although this increase was small compared with that obtained when gravity was considered), followed by a continuous decrease in the value of a_x as St_K was increased from 1.76 to 11.8. This non-monotonous variation of a_x with St in the absence of gravity was also found in the numerical study of Zamansky et al. (2011), who showed that in the near-wall, non-isotropic turbulence, the maximum value of a_x increased when St^+ increased from 1 to 5, and then decreased for higher St^+ (up to $St^+ = 25$). The results of the two numerical investigations indicate that other mechanisms in addition to gravity can decelerate the particles and increase a_x. In particular, the effects of particle-wall interaction on acceleration statistics of inertial particles must be investigated.

The effects of particle-wall interactions have been studied experimentally under quiescent and flowing conditions. Joseph et al. (2001) measured the particle restitution coefficient (e), defined as the ratio of particle velocity immediately after and before its collision with the wall, in fluids with different viscosities. Their experimental setup consisted of a spherical particle attached to a string. This pendulum was released from different initial angles and moved through a quiescent liquid until the particle hit a vertical wall with an impact angle of 90˚. They defined the impact Stokes number, $St_v=\rho_p d_p V_0/(9\mu)$, based on the particle's wall-normal impact velocity (V_0), particle diameter (d_p), particle density (ρ_p) and dynamic viscosity of the fluid (μ). In their experiments, particle rebound did not occur (i.e. e = 0) when St_v was below a critical value (St_v ~ 10). At values $10 < St_v < 30$, the coefficient e rapidly increased with increasing St_v (Joseph et al. 2001); however, with further increase in St_v, values of e increased more slowly and eventually asymptotically approached the value for dry collision (i.e. collision in air). The dependency of e on St_v is also reported by Gondret et al. (2002), Stocchino & Guala (2005), and Legendre et al. (2006). Some other quiescent fluid studies also showed that e depends on the impact angle (θ_i) which is defined as the angle between particle trajectory and the wall. For example, Salman et al. (1989) tested particle-wall collisions in air and showed that an increase in θ_i reduced the wall-normal restitution coefficient (e_V, defined as the ratio of the wall-normal velocity of a particle after and before the collision). This reduction was also observed by Joseph et al. (2004). The dependence of e on θ_i in a turbulent flow of air was investigated by Sommerfeld & Huber (1999). They measured e, θ_i, and rebound angle (θ_r) of spherical particles in air flowing through a horizontal rectangular channel. Their results also showed the reduction of e with increasing θ_i. This reduction is also reported in a recent study by Sommerfeld & Lain (2018) for non-spherical particles in a turbulent air flow.

The dependence of e on θ_i shows the important role this angle plays in particle-wall collision in turbulent flows. The motion of particles in non-isotropic turbulent flows strongly depends on the turbulent structures interacting with the particles (Kaftori et al. 1995a, b; Marchioli & Soldati 2002; Kiger & Pan 2002). For example, sweep and ejection motions affect particles flux toward and away from the wall (Nino & Garcia 1996; Soldati 2005), and quasi-streamwise vortices are known to cluster small particles along low-speed streaks (Nino & Garcia 1996). Knowledge of the distributions of θ_i and e in a particle-laden turbulent flow is a key factor for modeling particle-wall interactions (Tsuji et al. 1987; Sommerfeld & Huber 1999; Kosinski & Hoffman 2009; Sommerfeld & Lain 2018).

In this study, we applied a time-resolved three-dimensional particle tracking velocimetry (3D-PTV) based on the shake-the-box (STB) algorithm of Schanz et al. (2016) to extract the Lagrangian trajectory of particles. This state-of-the-art PTV method uses a few initial time steps to predict the particle location based on a polynomial fit of the particle trajectory. This prediction is corrected using an image matching technique, which involves "shaking" the particles about their predicted location (Wieneke 2013). As a result of this combined algorithm, accurate tracking of particles from 2D images with up to 0.08 particles per pixel (ppp) has become possible (Schröder et al. 2015; Schanz et al. 2016). The STB technique is used here to obtain trajectories, velocity and acceleration of inertial particles in a horizontal turbulent channel flow. The trajectories are also used to investigate collision of the inertial particles with a wall, with specific attention paid to θ_i, θ_r, and particle momentum exchange with the wall. The experimental setup, data processing, and the properties of the turbulent flow and the inertial particles are described in § 2. The accuracy of the measurement system and the processing algorithm is verified by comparing the measured velocity and acceleration statistics with DNS of unladen flow from Moser et al. (1999) and Yeo et al. (2010) in § 3. The velocity and acceleration fields of the inertial particles are investigated in § 4. A quadrant analysis is performed in § 5 to study the contribution of turbulent motions to Reynolds stresses and acceleration of the inertial particles. The collision of the particles with the wall is investigated in § 6 using conditional averaging of particle velocity and acceleration based on the turbulent motions of particles and θ_i.

2. Experimental setup

The experiments are conducted in a closed flow loop with a transparent test-section constructed specifically for 3D-PTV measurements. The ability of the STB algorithm in simultaneous recording of the trajectories of a large number of particles across the measurement domain with high accuracy makes it a desirable method for the Lagrangian tracking of particles (Toschi & Bodenschatz 2009) and measurement of their acceleration in turbulent particle-laden flows. Descriptions of the flow facility, the test conditions, and the 3D-PTV system are provided in the following sections.

2.1 *Flow facility*

The closed horizontal flow-loop consisted of 2-inch (nominal) diameter pipe and included a 3 m long rectangular test section as shown in figure 1. The test cross-section had dimensions of (W×2H) = 120×15 mm^2 (where H is the channel half-height) and thus a hydraulic diameter of D_h = 26.7 mm. The test-section was connected to the pipes using two gradual transition sections with 30 cm length. The measurement location was 220H from the entrance of the rectangular section to ensure fully developed turbulent flow. The test-section had glass walls for optical access, which were also removable to calibrate the 3D-PTV system. A centrifugal pump (LCC-Metal, GIW Industries Inc.) circulated the flow inside the flow-loop. The flow rate and the temperature were measured using a Coriolis flowmeter (Micro Motion F-Series, Emerson Industries) with mass flow accuracy of 0.2%. The pump was isolated from the test section using rubber joints so that vibrations from the pump or flow-loop do not affect the optical measurements. The temperature of the flow was kept constant at 20˚C for all the measurements using a double-pipe heat exchanger. All experiments were performed at Re_H = 14,600, based on the channel height and the bulk velocity across the channel (U_b = 0.98 m/s), which corresponded to a mass flow rate of 1.76 kg/s. The friction velocity of the unladen flow was u_τ = 0.0548 m/s, meaning the friction Reynolds number of $Re_\tau = u_\tau H/\upsilon$ = 410. The wall-normal unit was λ = 18.3 µm, estimated from the 3D-PTV measurements as discussed in § 3. The main flow parameters are shown in table 1.

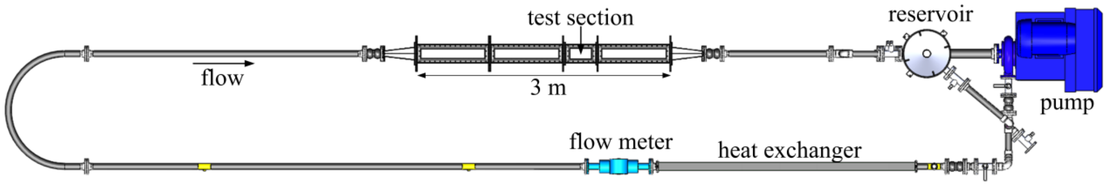

FIGURE 1. The 18 m (length) by 0.054 m (diameter) flow loop used in the present study, which includes a transparent channel with a rectangular test section used for optical measurements.

Re_τ	Re_H	U_b, m/s	u_τ, m/s	λ, µm
410	14,600	0.98	0.0548	18.3

TABLE 1. The flow parameters describing the unladen flow. The inner scaling is calculated from the velocity profile measured using the 3D-PTV technique.

2.2 *Particle-laden flow characteristics*

The particle-laden flow consisted of narrowly sized glass beads with mean diameter of d_p = 125 µm and density of ρ_p = 2.5 g/cm^3 dispersed in water at volumetric concentration of C_v = 0.03%, equivalent to mass fraction of C_m = 0.1%. For these glass beads and the test conditions under which they were studied, St^+ = 3.9, where St^+ was defined as the ratio of the bead relaxation time to the inner time-scale of the flow (t_p/t_f). The time-scales were estimated as $t_p = (\rho_p\text{-}\rho_f)\, d_p^2/18\mu$ and $t_f = \upsilon/u_\tau^2$ where ρ_f and υ are the density and kinematic viscosity of the fluid, respectively. The St can also be determined based on the Kolmogorov time scale, t_K. The Kolmogorov time scale is estimated as $t_K = (\upsilon/\varepsilon)^{0.5}$ where $\varepsilon = C_\mu^{0.75}k^{1.5}/l_m$. Here, k is the turbulent kinetic energy, l_m is turbulent mixing length, and C_μ = 0.09 (Milojevié, 1990). Turbulent mixing length can be estimated using the $l_m = \kappa y(1\text{-}y/(2H))^{0.5}$, where κ = 0.4 is the von Karman constant (Prandtl 1932). Based on the values of k and l_m at y = 4 mm (the farthest available data point from the bottom wall), t_K is about 5 ms. Therefore, the lower bound of the glass bead's St_K in the measurement domain is 0.2.

The Reynolds number for glass beads can be defined as $Re_p = U_s d_p/\upsilon$, where U_s is the streamwise slip velocity of the beads. From the 3D-PTV measurement (discussed in § 3), the mean streamwise velocity of unladen flow, $\langle U_f\rangle$, and the beads mean velocity, $\langle U_p\rangle$, can be measured. These values are used to estimate U_s as $|\langle U_f\rangle\text{-}\langle U_p\rangle|$. Using this equation, the maximum Re_p in the measurement domain is about 11.2. This maximum Re_p is an order of magnitude less than the threshold of Re_p = 110, suggested for vortex shedding from spherical particles (Hetsroni 1989). The properties of the glass beads studied here are summarized in table 2. It should be expected that the inertia will have a considerable effect on the dynamics of the glass beads since $St^+ > 1$ (Aliseda et al. 2002). Particle-particle collisions were not expected to play a significant role at this concentration (Elghobashi 1994).

d_p, µm	$d_p^+ = d_p/\lambda$	$r_\rho = \rho_p/\rho_f$	C_v, %	C_m, %	V_t, m/s	Re_p	t_p, ms	St^+
125	6.8	2.5	0.03	0.1	0.013	11.2	1.30	3.9

TABLE 2. Properties of the glass beads used as inertial particles tested in the present study.

From comparison of C_m (0.1%) and d_p^+ (6.8) of the current investigation with previous studies, the effect of glass beads on the turbulent structures of the fluid phase is expected to be negligible, i.e. a marginal two-way coupling. The experimental results of Kulick et al. (1994) showed that 90 µm glass beads with C_m of 2% and d_p^+ of 3 had a negligible effect on the turbulent intensity of the carrier phase. The numerical analysis of Nasr & Ahmadi (2007) for particles with d_p^+ of 2.2 and C_m = 2% also showed a negligible change of the flow turbulent kinetic energy and dissipation. In Kulick et al. (1994) and Nasr & Ahmadi (2007), the carrier phase was air, which has a higher r_ρ relative to the current study. Therefore, the smaller r_ρ of the present investigation is expected to result in an even smaller modulation of flow turbulence (Yu et al. 2017). Regarding the finite size of the beads, DNS of Luo et al. (2017) for particles with d_p^+ of 11.3 (without point-particle assumption), r_ρ of 3.3, and C_v of 0.1% showed a negligible effect on fluid turbulence. This observation was made in spite of turbophoresis and a larger near-wall particle concentration in their study.

2.3 *Lagrangian 3D-PTV measurements*

A time-resolved 3D-PTV system was used to obtain glass bead trajectories based on the Lagrangian tracking method of Schanz et al. (2016), which is known as shake-the-box (STB). The system consisted of four CMOS high-speed cameras (Phantom v611) with a pixel size of 20×20 µm^2 operated at a cropped sensor size of 1024×608 pix. Each camera was equipped with a Scheimpflug adaptor and a Sigma SLR objective lens with a focal length of f = 105 mm at an aperture size of f/16. The magnification of the imaging system was 0.41 at a digital resolution of 0.049 mm/pix and depth-of-field of 7.9 mm. The cameras were arranged in a plus-like configuration with solid-angle of ~35° from the y-axis as shown in figure 2. The cameras were synchronized with a dual-cavity Nd:YLF laser (DM20-527, Photonics Industries) through a high-speed controller (HSC v2, LaVision GmbH) controlled by DaVis 8.4 (LaVision GmbH). The laser had a wavelength of 527 nm and each cavity had maximum energy of 20 mJ per pulse (at frequency of 1 kHz). A combination of cylindrical and spherical lenses was used to collimate the laser beam into a sheet with cross-section of 50×4 mm^2 in the streamwise (x) and wall-normal (y) directions. The laser sheet entered the test section from the sidewall, passed parallel to the bottom wall, and exited from the opposite sidewall (from top to bottom in figure 2). To increase the laser intensity a mirror was used on the opposite side (after the test section) to reflect the laser back into the measurement volume. Two knife-edges were used outside the sidewalls to form a top-hat intensity profile and limit the laser sheet in the region $0 \le y \le 4$ mm. The y-axis points in the wall-normal direction from the bottom wall toward the top wall with $y = 0$ at the bottom wall. The center of the coordinate system was located at the center of the bottom wall of the test section as shown in figure 2. The flow was in the positive x direction and the z-axis indicates the spanwise direction.

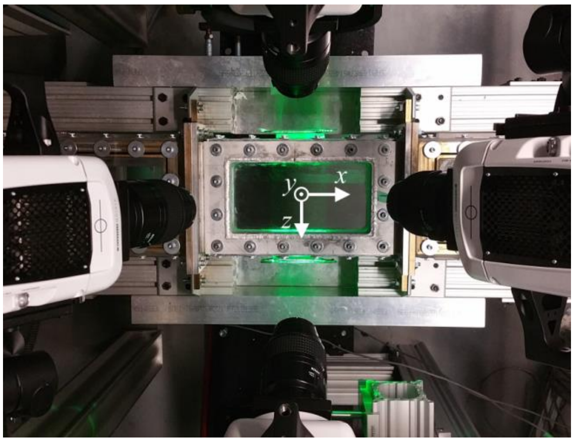

FIGURE 2. An image of the high-speed 3D-PTV system showing the four cameras imaging the test section in a plus-like configuration. The laser sheet is reflected back into the test-section using a mirror to increase the light intensity and to equalize the image intensity of the cameras in backward and forward scattering orientations (Ghaemi & Scarano 2010).

A 3rd order polynomial function was obtained using a 3D target to calibrate the imaging system and map the physical coordinate system on the image coordinate system. The calibration errors were reduced to 0.05 pixel by applying volume self-calibration algorithm of Wieneke (2008) in DaVis 8.4 (LaVision GmbH). The average disparity error in the whole measurement domain was about 0.01 pixel with standard deviation of 0.01 pixel. The reported disparity error is an order of magnitude smaller than the maximum recommended value of 0.1 pixel by Wieneke (2008). The measurement volume was 50×4×30 mm^3, which was equivalent to 1024×82×608 pix^3. Image acquisition was at a speed of 6 kHz for the unladen flow measurements and 10 kHz for particle-laden measurements. In each case, the system was set to single-frame mode with simultaneous emission of the two laser cavities. The acquisition rate was higher for the particle-laden flow tests to better resolve the bead-wall collision process. The time interval between laser pulses was 167 and 100 μs for the unladen and bead-laden measurements, respectively, or about half and one-third of the inner time-scale of the flow (t_f = 337 μs). The specifications of the 3D-PTV setup are detailed in table 3. The unladen flow was seeded with 2 μm silver-coated tracers (SG02S40 Potters Industries) with density of 3.6 g/cm^3. The tracers had an image size of 3 pixels, their volumetric number density was 3 tracer/mm^3, and the number density of the tracers in the images was 0.024 tracer per pixel. The maximum displacement of the tracers for unladen flow measurements did not exceed 4 pix between two consecutive images. In the bead-laden flow (no tracer), the 125 µm glass beads had a Gaussian intensity profile and image diameter of ~3 pixels. The number density of beads was 0.825 beads per cubic millimetre at volumetric concentration of 0.03%. The number density of beads in the images was 0.008 beads per pixel. The maximum displacement of beads was ~2 pix between two consecutive images.

CCD sensor size (cropped)	1024×608 pix
Illuminated volume (x, y, z)	50×4×30 mm^3
Magnification	0.41
Digital resolution	0.049 mm/pix
f / #	16
Depth of field	7.9 mm
Acquisition frequency of unladen flow	6 kHz
Acquisition frequency of laden flow	10 kHz

TABLE 3. Specifications of the 3D-PTV system used in the present study.

After recording the images, the minimum intensity of the ensemble of images was subtracted from each image to remove the background. The signal-to-noise ratio of the images was also improved by subtracting minimum intensity within a kernel of five pixels from each pixel, and normalizing it using the average intensity within a kernel of 50 pixels. The image intensity of the cameras was also normalized with respect to each other, and a Gaussian filter with kernel of 3×3 pixel was applied. An optical transfer function (OTF) was obtained and applied in every step of iterative particle reconstruction and the shaking as described by Schanz et al. (2016). The data were processed using the STB algorithm (Schanz et al. 2016) in DaVis 8.4 (LaVision, GmbH) to determine the 3D trajectory of each tracer in unladen flow and each bead in bead-laden flow. In this algorithm, the 3D location of each particle is initially determined based on particle intensity, an allowed triangulation error, and a prediction of particle location from the previous images. The deviation of the predicted location is corrected by shaking the particle around the predicted location in small increments, and calculating the residual intensity following the iterative particle reconstruction method (Wieneke 2013). The allowed triangulation error was 0.5 pix (24.5 µm) and the shake width was 0.1 voxel. To avoid spurious results, the maximum allowable displacement was 4 voxels for the tracers and 3 voxels for beads. The maximum absolute and relative changes in the particle displacement between two consecutive images were limited to 2 pixel and 50%, respectively. The STB algorithm detected about 300 tracer trajectories and about 50 bead trajectories per image for the unladen and the bead-laden experiments, respectively. Visualization of a sample trajectory of a bead is presented in figure 3 showing its wall-normal location normalized by the inner length-scale ($y^+ = y/\lambda$) as a function of time, which is also normalized by the inner time-scale ($t^+ = t/t_f$). The bead slides along the wall over time period of $115 \leq t^+ \leq 130$ and the sharpest wall collision angle is at $t^+ \approx 200$.

The location of the lower wall was obtained using the minimum intensity of all the images. This minimum image was mostly dark, except for a few glare points due to the reflection of laser from the wall. To find the 3D position of the glare point, i.e. wall location, the minimum image was reconstructed into the 3D domain using the multiplicative algebraic reconstruction technique (MART) in DaVis 8.4 (Elsinga et al. 2006). The average intensity of the glare points was determined in each reconstructed x-z plane. A Gaussian distribution was fitted on the wall-normal variation of glare points intensity to obtain the wall location with subpixel accuracy. Based on this procedure the uncertainty of the wall-location is 0.1 pixel (4.9 µm) which is equivalent to 0.27λ.

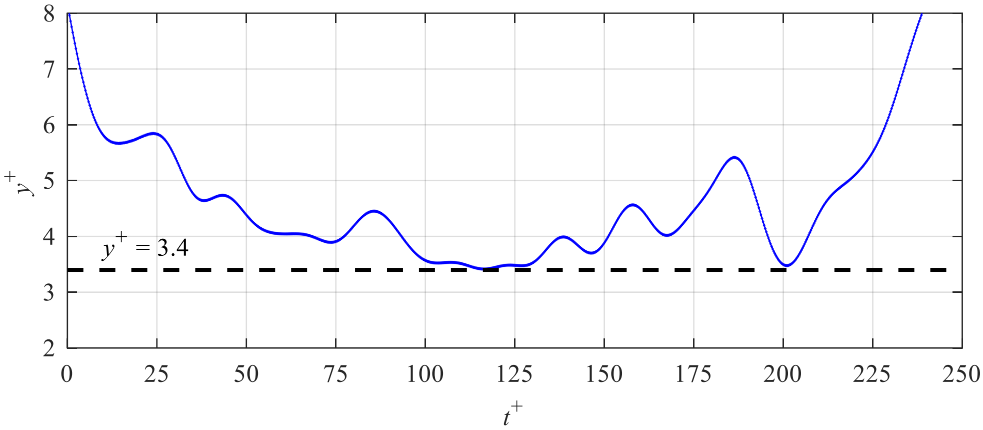

FIGURE 3. Visualization of a bead trajectory showing multiple interactions with the wall. The dashed line shows $y^+ = d_p^+/2$ which is the minimum y that the center of the bead can reach. The bead is sliding on the wall at $115 \leq t^+ \leq 130$ and has a relatively steep-angle collision with the wall at $t^+ \approx 200$.

The streamwise, wall-normal, and spanwise instantaneous velocities (U, V, W), velocity fluctuations (u, v, w), instantaneous acceleration (A_x, A_y, A_z), and rms of acceleration components (a_x, a_y, a_z) were determined from the 3D Lagrangian trajectories. The velocity and acceleration were obtained by applying a quadratic regression fit with temporal kernel of 4.5 ms (~$13t_f$) on either the tracer or the bead trajectories. The kernel size was evaluated by comparing the velocity and acceleration statistics of unladen flow with the DNS results of Moser et al. (1999) and Yeo et al. (2010). The effect of the temporal kernel on the rms of acceleration values was evaluated following the method of Voth et al. (2002) and Gerashchenko et al. (2008), and is shown in appendix A. The velocity and acceleration data were averaged in the streamwise and spanwise direction (in addition to time) due to homogeneity of the flow field in these directions. The ensemble averaged quantities are indicated using the $\langle\ \rangle$ symbol. The wall-normal dimension of the averaging bins was one wall unit (λ) for the unladen flow. The bin size was larger and equal to the diameter of a bead (6.83λ) for the bead-laden flow. More than 9×10^6 tracer trajectories for unladen flow from 27,000 images (at 6 kHz) and about 2.3×10^6 bead trajectories in the bead-laden flow from 45,000 images (at 10 kHz) were obtained using the STB algorithm. The convergence of the velocity and acceleration statistics of beads at $y^+ = 16.7$, where $\langle u^2\rangle$ was a maximum, is investigated in appendix B. The random errors in measurement of velocity and acceleration statistics of glass beads were calculated based on the standard deviation of the last 20% of data collected at this location and are presented in table 4. The mean duration of bead trajectories is relatively constant and is about 20 ms for $y^+ > 20$. For smaller y^+, the mean trajectory duration gradually shortens to about 13 ms.

$\langle U \rangle$	$\langle V \rangle$	$\langle u^2 \rangle$	$\langle v^2 \rangle$	$\langle w^2 \rangle$	$\langle uv \rangle$	$\langle A_x \rangle$	$\langle A_y \rangle$	a_x	a_y	a_z
0.1%	0.7%	0.5%	0.3%	0.3%	0.2%	0.7%	0.3%	0.1%	0.3%	0.2%

TABLE 4. Random errors of the velocity and acceleration statistics of glass beads based on the standard deviation of the last 20% of data collected at $y^+ = 16.7$. The details are available in appendix B.

3. Unladen turbulent channel flow

The unladen flow field statistics and the uncertainty of the 3D-PTV technique are evaluated by comparing the velocity statistics with the DNS results of Moser et al. (1999) at $Re_\tau = 395$ and the acceleration statistics with a separate DNS study of Yeo et al. (2010) at $Re_\tau = 408$. The normalized mean streamwise velocity (U^+), where $U^+ = \langle U \rangle / u_\tau$, is shown here as figure 4(a). The 3D-PTV measurement agrees well with the DNS results of Moser et al. (1999) from the first data point at $y^+ = 3.4$ in the viscous sublayer up to the border of the measurement volume at $y^+ = 218$ ($y = 4$ mm) in the logarithmic region. The logarithmic law ($U^+ = 1/\kappa \ln(y^+) + B$) with $\kappa = 0.4$ and $B = 5.2$ is also shown in this figure.

The non-zero components of the Reynolds stress tensor, $\langle u_i u_j \rangle$, determined from 3D-PTV measurement, are shown in figure 4(b). The mean streamwise Reynolds stress profile, $\langle u^2 \rangle$, at the near-wall region of $y^+ \leq 12$ is slightly larger (4% in the peak) than the DNS results, and the maximum is also closer to the wall by ~2λ. The difference can be partly attributed to the fact that the measurement was made at $Re_\tau = 410$ which results in a thinner inner layer and slightly larger values of $\langle u^2 \rangle / u_\tau^2$ than the Moser et al. (1999) simulation, where $Re_\tau = 395$. The profiles of mean wall-normal Reynolds stress, $\langle v^2 \rangle$, and mean spanwise Reynolds stress, $\langle w^2 \rangle$, overlap the DNS results and reach their maximum values at $y^+ = 70$ and 40, respectively. The mean Reynolds shear stress, $\langle uv \rangle$, also agrees well with the DNS data, and the minimum value is reached at $y^+ = 35$. The good agreement of the measurement with the DNS results also provides evidence indicating that (i) fully developed channel flow is established and (ii) the 3D-PTV can resolve the mean and second-order velocity statistics in the region $3.5 \leq y^+ \leq 218$.

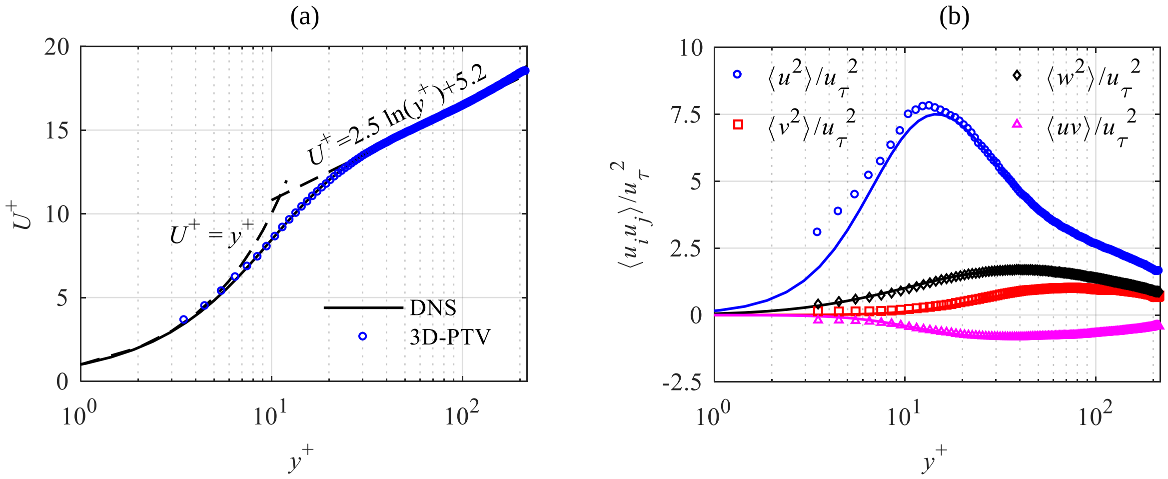

FIGURE 4. Comparison of 3D-PTV measurement of (a) mean streamwise velocity, and (b) non-zero components of Reynolds stress tensor in unladen flow at $Re_\tau = 410$ (symbols) with the DNS results of Moser et al. (1999) at $Re_\tau = 395$ (solid lines).

The ability of the 3D-PTV technique in resolving the mean and second-order acceleration statistics is investigated by comparing the results of the measurement made for the unladen flow with the DNS results of Yeo et al. (2010) at $Re_\tau = 408$. The profiles of normalized mean streamwise acceleration $A_x^+ = \langle A_x \rangle/(u_\tau^3/\upsilon)$ and mean wall-normal acceleration, A_y^+, and mean spanwise acceleration, A_z^+, are presented in figure 5(a) for the unladen flow. The measurements of A_x^+ and A_y^+ show good agreement with the DNS. At the locations where the minimum value of A_x^+ and maximum value of A_y^+ occur (y^+ = 8 and 18, respectively), the difference between the experimental and simulation results is about 4%. At $y^+ < 35$, A_x^+ is negative, which indicates flow deceleration. Yeo et al. (2010) attributed the negative value of A_x^+ in the near-wall region mainly to the viscous force within the solenoidal acceleration ($\equiv \upsilon\partial^2\langle U \rangle/\partial y^2$). The negative A_x^+ at $y^+ < 35$ is also expected because $\langle A_x \rangle \equiv \partial\langle uv \rangle/\partial y$ (Chen et al. 2010). As it is well-known and seen in figure 4(b), $\partial\langle uv \rangle/\partial y < 0$ in this region. At $y^+ < 70$, A_y^+ is positive as shown in figure 5(a). This agrees with the DNS results of Yeo et al. (2010) at Re_τ = [180, 408, 600] and the DNS results of Zamansky et al. (2011) at $Re_\tau = 587$. The positive values of A_y^+ at $y^+ < 70$ is also expected since $\langle A_y \rangle \equiv \partial\langle v^2 \rangle/\partial y$ (Chen et al. 2010) and $\partial\langle v^2 \rangle/\partial y$ is positive up to $y^+ \approx 70$ as observed in figure 4(b). The variation of A_y^+ with y^+ also agrees with variation of $\partial\langle v^2 \rangle/\partial y$ with y^+ in figure 4(b). However, the trend of the values of A_y^+ measured for the present study is not in agreement with the DNS results of Lavezzo et al. (2010) at $Re_\tau = 300$ or Yu et al. (2016) at $Re_\tau = 150$, who reported negative A_y^+ values near the bottom wall of horizontal channel flows. The positive A_y^+ in the inner layer is attributed to the irrotational component of $\langle A_y \rangle$ ($\equiv -\partial\langle p \rangle/\rho\partial y$) that accelerates the flow upward toward the axis of rotation of quasi-streamwise vortices (Lee et al. 2004; Lee & Lee 2005; Yeo et al. 2010). The rotational motion of the quasi-streamwise vortices provides a mean low-pressure core at $y^+ \approx 20$ (Kim et al. 1987). This is consistent with the location of maximum value of A_y^+ at $y^+ = 18$ in figure 5(a). The trends of the wall-normal variation of $\langle A_x \rangle$ and $\langle A_y \rangle$ of the unladen flow in current study are also consistent with experimental and DNS results of Stelzenmuller et al. (2017). For a spanwise homogeneous flow, A_z^+ is expected to be zero. The maximum deviation of A_z^+ from zero is about 7.3×10^{-4} and occurs at $y^+ = 4.5$, which is an indication of small measurement uncertainty.

The normalized rms of the acceleration components are presented in figure 5(b) as $a_i^+ = a_i/(u_\tau^3/\upsilon)$, where i = x, y, and z, and are compared with the results of the simulations of Yeo et al. (2010). There is a good agreement between the measured and the DNS values of a_x^+, with a maximum difference of about 6% at the maximum value of a_x^+, which occurs at $y^+ = 6$. The measured values of a_y^+ are in accord with the DNS profiles at $y^+ \geq 30$, with a difference of about 2% for the maximum value of a_y^+ (at $y^+ = 30$). At $y^+ < 10$, the measured a_y^+ deviates from DNS while the profile of a_x^+ follows the DNS. This is due to the higher relative error in y (and z) directions compared with x direction; the particles displacement in y (and z) is an order of magnitude smaller than that in x direction. The maximum values of a_y^+ and a_z^+ are in the buffer layer (further away from the wall than the maximum value of a_x^+), which suggests that they are pressure-driven due to vortical structures (Yeo et al. 2010). It is also noticeable in figures 5(a) and (b) that the magnitudes of a_x^+ and a_y^+ are greater than the magnitudes of A_x^+ and A_y^+, respectively, showing the intermittency of the events with high acceleration in the flow.

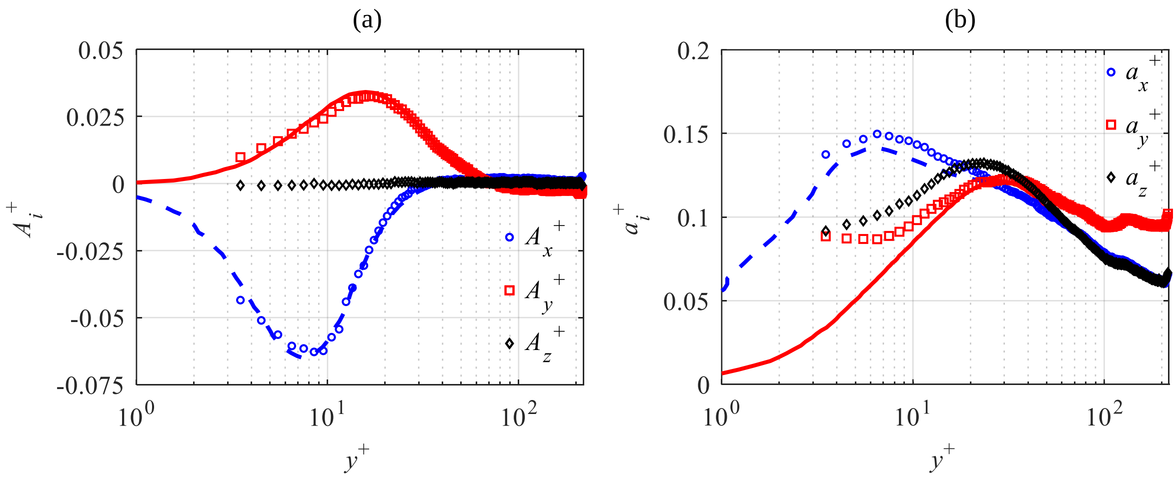

FIGURE 5. 3D-PTV measurement (symbols) of (a) mean acceleration, and (b) rms of acceleration for the unladen flow at $Re_\tau = 410$. The results are normalized with inner scaling and compared with the DNS results of Yeo et al. (2010) at $Re_\tau = 408$ (dashed and solid lines).

4. Bead-laden turbulent channel flow

The distribution of beads' number density in the near-wall region is presented in figure 6. This distribution is determined based on the number of beads in each bin (N) divided by the average number of beads across all the bins (N_{avg}). The wall-normal location is normalized by λ. The averaging bin size for beads is equal to d_p and the first data point is obtained at the center of the first bin immediately after the wall (i.e. at $y^+ = 3.4$). For this analysis, all the detected beads are considered, as no limitation is imposed on their trajectory length. As expected, the concentration of glass beads is higher close to the wall due to the gravity. The figure also demonstrates that local near-wall number density can be up to 2.2 times larger than the average number density within the measurement domain, i.e. $y^+ < 218$ region. The relatively small increase of local number density in the vicinity of the wall suggests that modulation of the liquid phase turbulence by the beads is small.

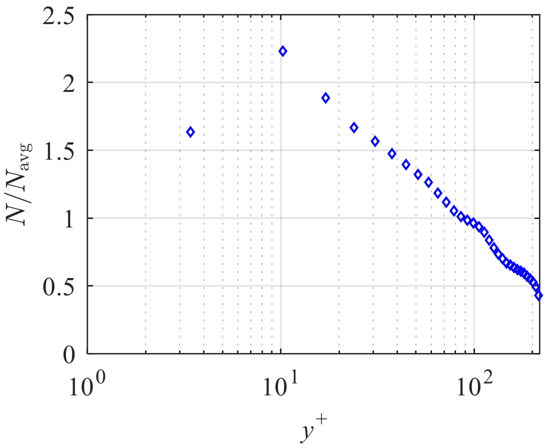

FIGURE 6. The normalized number density of glass beads in the near-wall region.

The velocity and acceleration statistics of glass beads obtained from the 3D-PTV measurement at $Re_\tau = 410$ are also investigated in this section. The velocity statistics are normalized using u_τ, and the acceleration statistics are normalized using u_τ^3/υ. The U^+ profiles of beads and the unladen flow are compared in figure 7(a). The bead velocity is greater than that of the unladen flow at $y^+ <10$ as the no-slip boundary condition does not apply to the beads. As a result, $\langle U_f\rangle$-$\langle U_p\rangle$ is negative; specifically, it is -0.09 m/s at $y^+ = 3.4$ which is about 10% of the bulk velocity. At $y^+ >10$, the bead velocity is lower than that of the unladen flow. A similar observation was reported by Shao et al. (2012) and Yu et al. (2016) and is associated with the larger inertia of beads (compared with that of the liquid phase). The trend of the U^+ profile is consistent with the results presented by others including Kussin & Sommerfeld (2002), Shao et al. (2012), and Yu et al. (2016) for different values of Re_τ and St. The mean wall-normal velocity of unladen flow and glass beads are also normalized by u_τ as $V^+ = \langle V\rangle/u_\tau$, and presented in figure 7(b). The value of V^+ is close to zero for unladen flow in the whole measurement domain. However, glass beads have a small negative V^+, showing their motion toward the lower wall. Therefore, the gravitational settling of beads is not totally balanced by turbulence diffusion. The former gradually accumulates the beads close to the wall, as seen in figure 6.

The normalized non-zero components of the Reynolds stress tensor of beads and the unladen flow are compared in figure 7(c), showing similar trends and approximately the same peak locations for the associated components. Beads have larger $\langle u^2\rangle$ in comparison with the unladen flow. Due to inertia, the glass beads can maintain their velocity for a longer time, and therefore over a longer wall-normal distance, relative to the fluid motions. As a result of this larger diffusion, a wider distribution of bead velocity, i.e. a larger velocity fluctuation, is observed (Shokri et al. 2017). The maximum of the absolute value of $\langle uv\rangle$ of beads, $|\langle uv\rangle|_{max}$, is about 30% larger than it is for the unladen flow, which indicates a greater correlation between their u and v and turbulence production. Shokri et al. (2017) compared the measured $\langle uv\rangle$ of inertial beads with unladen flow in an upward turbulent vertical pipe flow. Their results showed that the $|\langle uv\rangle|_{max}$ of beads (with St^+ values of 3.9 and 7.7) was about 30% larger than the unladen flow. However, at $St^+ = 14$, $|\langle uv\rangle|_{max}$ became 27% smaller than $|\langle uv\rangle|_{max}$ for the unladen flow, indicating that the difference between $|\langle uv\rangle|_{max}$ of beads and unladen flow is strongly dependent on St^+. The DNS results of Yu et al. (2017) showed a similar effect of St on the difference between $|\langle uv\rangle|_{max}$ of particles and unladen flow in horizontal turbulent channel flows.

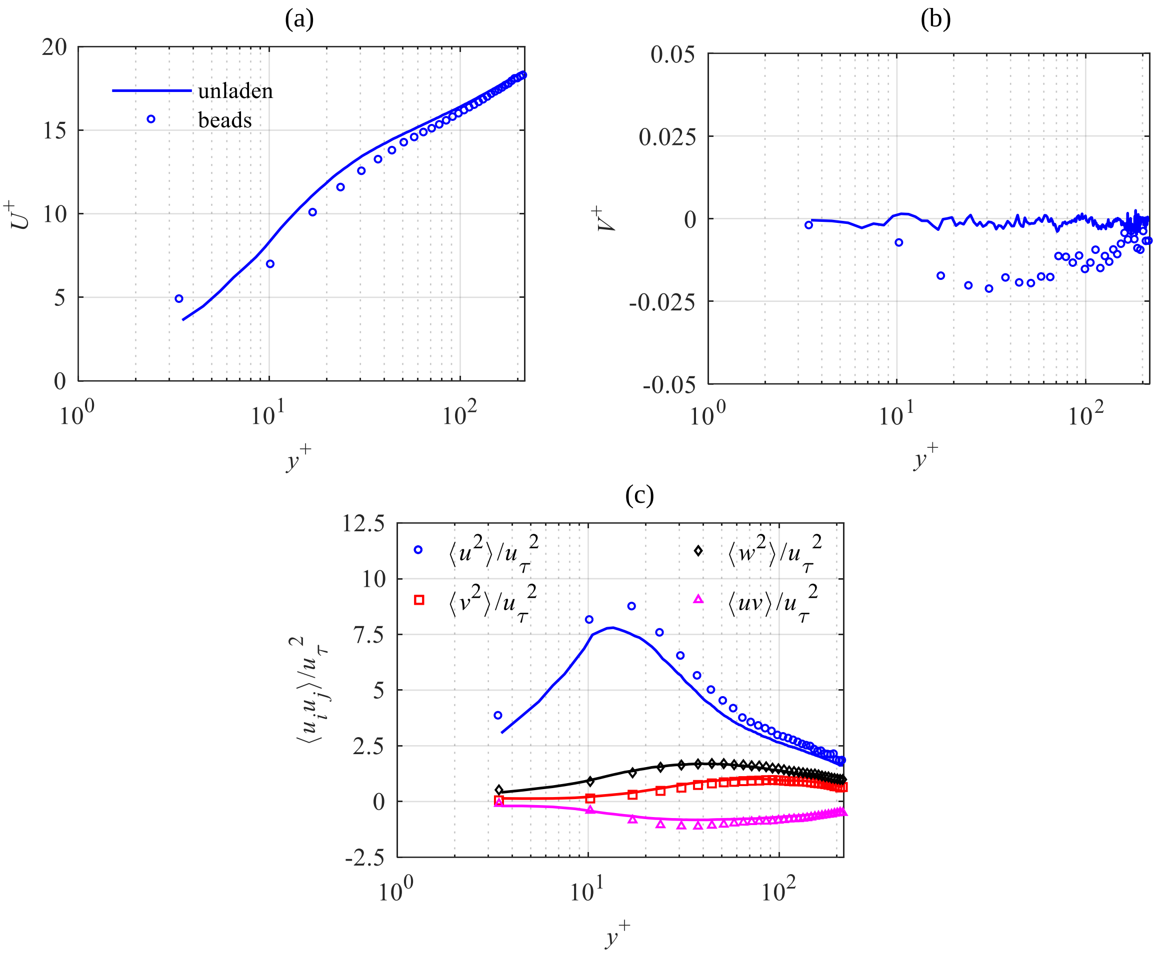

FIGURE 7. Comparison of 3D-PTV measurements of (a) mean streamwise velocity, (b) mean wall-normal velocity, and (c) mean Reynolds stresses of beads (symbols) with the same parameters for the unladen flow (solid lines) at $Re_\tau = 410$.

The normalized mean and rms of beads acceleration are compared with the numerical results of Zamansky et al. (2011) in figure 8. This numerical simulation was carried out for small particles (d_p^+<1) with a large density ratio (r_ρ =770). For this flow regime, Zamansky et al. (2011) assumed point-particles, and the steady-state drag was the only force taken into account for the solid phase equations of motion. The effect of the added-mass, Basset, Saffman, Magnus, and gravity forces were neglected. In the experiment, d_p^+ is larger and r_ρ is smaller. However, the numerical simulation is performed with St^+ = 5 and Re_τ = 587, which are close to the St^+ and Re_τ of the current experiment. It should be noted that the comparison with the numerical simulation is not carried out here to evaluate the uncertainty of the 3D-PTV or the validity of the assumption for the numerical simulation. Here, we qualitatively compare the acceleration statistics of the experiment and the numerical simulation. The comparison also allows us to evaluate if the point-particle assumption is valid for the flow condition of the experiment. To the authors' knowledge, this simulation is the most comparable to the results of the current study, especially when one considers that mean and rms of acceleration are needed for the comparison.

From the A_x^+ profile of beads, presented in figure 8(a), bead deceleration (A_x^+ < 0) occurs at y^+< 20 with the minimum value of A_x^+ occurring at $y^+ \approx 10$. Bead deceleration is attributed to the slower viscous-dominated flow of the surrounding near-wall fluid and the interaction of beads with the wall. It is notable that the location of the minimum value of A_x^+ is close to the location of the minimum value of $\partial\langle uv\rangle/\partial y$ for beads shown in figure 7(c). Lavezzo et al. (2010) used DNS of a particle-laden flow, with St_K = [0.87, 1.76, 11.8] to show that $\langle A_x\rangle$ and $\partial\langle uv\rangle/\partial y$ are related for inertial particles. The current experimental investigation also confirms this relation. The measured value at y^+ = 3.4 is A_x^+ = -0.038, while the numerical result at this location is A_x^+ = -0.019. This difference cannot be due to the different values of St^+; as shown by Zamansky et al. (2011), increasing St^+ from 1 to 5 does not considerably affect A_x^+ at this near-wall position. It also is not expected that the higher value of Re_τ in the numerical study compared with the measurement is the reason for the difference in A_x^+ at y^+ = 3.4. Yeo et al. (2010) showed that increasing Re_τ enhances the viscous force contribution and increases the deceleration; but this increment is negligible for $Re_\tau > 400$. The difference between the measured A_x^+ and the numerical result at $y^+ = 3.4$ is attributed to the larger particles, smaller r_ρ, and bead-wall collision in the experiment. In the present study, the location of $A_x^+ = 0$ for beads is at $y^+ \approx 20$, which is closer to the wall than was found by Zamansky et al. (2011). Comparison of the A_x^+ profiles for the solid-phase (figure 8(a)) and the unladen flow (figure 5(a)) shows that the two are different when $y^+>20$: the unladen profile is relatively constant at a small positive value while for beads there is a local maximum at $y^+ \approx 40$, just above the buffer layer where $\partial\langle uv\rangle/\partial y$ is also positive, as shown in figure 7(c). The difference is mainly associated with the acceleration of the beads that are ejected away from the wall. The region of positive A_x^+ overlaps with the logarithmic layer and indicates where fluid applies a net positive force on the particles to accelerate them. The streamwise velocity difference between glass beads and fluid results in a drag force (Crowe et al. 2012), which causes a local maximum of A_x^+ at $y^+ \approx 40$.

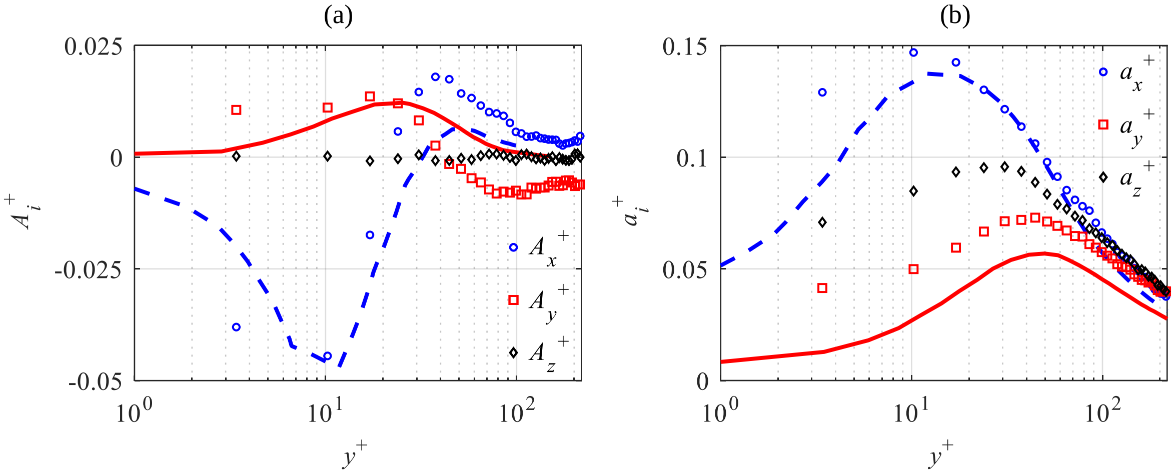

FIGURE 8. Comparison between measurement of normalized (a) mean acceleration, and (b) rms of acceleration components from the 3D-PTV (symbols) with the numerical results of Zamansky et al. (2011) at $Re_\tau = 587$ with $St^+ = 5$ (lines).

The maximum value of A_y^+ is found at $y^+ \approx 18$ of figure 8(a). This is the same location of the maximum value of $\partial\langle v^2\rangle/\partial y$, as shown in figure 7(c), as well as the location of the maximum A_y^+ for the unladen flow, as shown in figure 5(a). This location is also near the mean axis of rotation of quasi-streamwise vortices, which is found at about $y^+ \approx 20$ (Kim et al. 1987) where a minimum pressure is expected. The positive acceleration can be associated with the ejection motions of the fluid, which lift up the beads and transport them away from the wall (Kiger & Pan 2002). For particles moving toward the wall, their V should decrease to result in a positive A_y^+. In the region $18 < y^+ < 40$, A_y^+ decreases and becomes zero at $y^+ \approx 40$. Figure 8(a) shows that at $y^+ < 20$, A_y^+ of beads is larger than the A_y^+ reported by Zamansky et al. (2011). After the zero A_y^+ point, the effect of gravity becomes dominant and A_y^+ of beads becomes negative. The negative A_y^+ values were not observed in the numerical results of Zamansky et al. (2011) in which gravity was not considered. As expected, the A_z^+ of glass beads is almost zero in the whole measurement domain. The maximum deviation of A_z^+ from zero is about 8.5×10^{-4} at $y^+ = 17$.

Considering the rms of the bead acceleration in figure 8(b), the maximum value of a_x^+ of beads coincides with the location of the minimum value of A_x^+ in figure 8(a). The maximum value of a_x^+ is larger than those of Zamansky et al. (2011). For unladen flow, Yeo et al (2010) observed that as Re_τ increases from 408 to 600, the maximum value of a_x^+ increases by 3%. The numerical results of Zamansky et al. (2011) showed that the relationship between St^+ and a_x^+ is not monotonous: a_x^+ increased with increasing St^+ from 1 to 5, but decreased with further increases in St^+. The greater values of a_x^+ at $St^+ \sim 5$ compared to its values at the other St^+ in their simulations is associated with the balance between the particles' response to the surrounding fluid and their wall-normal dispersion. The wall-normal dispersion is expected to initially increase with increasing St^+, which results in acceleration/deceleration of beads when transported to different fluid layers, thereby increasing a_x^+. The maximum value of a_y^+ in the measurement is also greater than that of the simulation. Again, the difference between a_x^+ and a_y^+ of the current measurement and those reported by Zamansky et al. (2011) in the immediate vicinity of the wall is mainly associated with the larger particles and the smaller r_ρ in the experiment. The discrepancy suggests that the point-particle assumption can not be applied to the condition of the current experiment. The fully elastic particle-wall collision assumption applied in the numerical simulation and measurement noise can also contribute to the discrepancy in bead's acceleration rms in the immediate vicinity of the wall.

The probability density functions (pdf) of the components of the bead mean acceleration normalized with rms of total acceleration, a, taken at five different y^+, are presented in figure 9. As figure 9(a) shows, at y^+ = 3.4 and 10.2, the pdf of A_x is skewed towards negative A_x, which is consistent with the results of figure 8(a) and the pdfs produced from the measurements of Gerashchenko et al. (2010). It is conjectured that the negative skewness of the pdf is due to deceleration of beads by strong near-wall viscous forces and beads interaction with the wall. With increasing y^+, the viscous dominated deceleration reduces, and beads accelerate due to inertial forces. At y^+ = 17, the pdf is more symmetric. With further increases in y^+ to 44.3 and 98.8, the pdf becomes right-skewed, which shows more beads tend to have positive A_x.

The pdf of A_y shown in figure 9(b) has different behaviour than was described above for A_x. Close to the wall and up to y^+ = 44.3, the pdf is skewed right, indicating that more beads tend to have a positive A_y, which means the value of V of upward moving beads increases or the value of V of downward moving beads decreases. The positive A_y can be associated to several forces. As it was mentioned, ejection motions of the liquid phase are known to lift up and accelerate beads away form the wall (Kiger & Pan 2002). It is conjectured that the negative wall-normal pressure gradient also contributes to the positive A_y of the upward moving beads. This pressure gradient has been attributed to a region of high vorticity where there is a larger accumulation of quasi-streamwise vortex cores are located (Kim 1989; Yeo et al. 2010). In the high-shear near-wall region, glass beads can also experience a large Magnus force. For a downward moving bead, the value of V is hypothesized to decreases due to the wall-normal pressure gradient and the increasing pressure of the fluid layer between the bead and the wall, known as wall repulsive force (Feng et al. 1994). By increasing y^+, the effect of these forces reduces, and glass beads experience a negative acceleration due to gravity. At y^+ > 44.3, the A_y pdf is skewed to the negative side, indicating that a large number of the beads with upward motion slow down, and downward moving beads speed up under the effect of gravity. The pdf of spanwise acceleration in figure 9(c) is symmetric as expected.

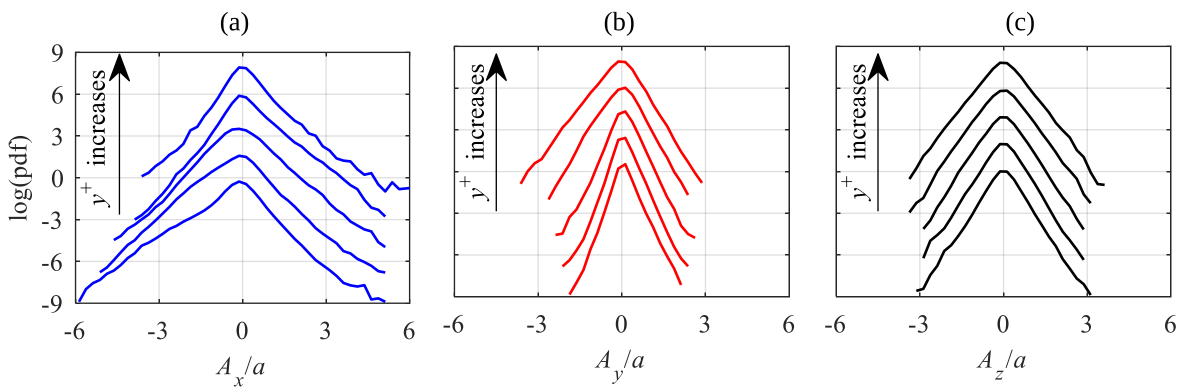

FIGURE 9. Probability density functions of mean (a) streamwise, (b) wall-normal, and (c) spanwise acceleration of beads. The curves in each plot, from bottom to top, correspond to y^+ = 3.4, 10.2, 17, 44.3, 98.8. The pdfs are each shifted up by two units of the vertical axis for clarity.

5. Quadrant analysis

The turbulent motion of the fluid and beads can be further analysed by plotting u and v in a quadrant plot. The motions described by the four quadrants are beginning with Quadrant 1 (Q_1), upward interactions with u > 0 and v > 0; ejections (Q_2) with u < 0 and v > 0; downward interactions (Q_3) with u < 0 and v < 0; and sweeps (Q_4) with u > 0 and v < 0, as originally proposed by Wallace et al. (1972). To evaluate the contribution of each quadrant to $\langle uv\rangle$, the motions of the unladen flow and beads are sampled based on u and v sign of each quadrant. The conditionally sampled data are averaged as indicated by $\langle uv\rangle_{Qi}$, where i varies from 1 to 4, referring to the four u-v quadrants. Figure 10(a) shows the contribution of Q_1 and Q_3 while figure 10(b) shows the contribution of Q_2 and Q_4. Based on the sign of $\langle uv\rangle$ and the positive $\partial\langle U\rangle/\partial y$ on the lower wall of the channel, the motions in Q_1 and Q_3 are associated with reduction of turbulence while motions represented in Q_2 and Q_4 generate turbulence. Comparison of figure 10(a) with figure 10(b) shows that there is poorer correlation of u and v for the beads in Q_1 and Q_3 than observed for the unladen flow; however, the beads with ejection and sweep motions in Q_2 and Q_4

have higher ⟨-uv⟩ compared with the unladen flow. Therefore, beads have a larger ⟨uv⟩ in the near-wall region which is consistent with their ⟨uv⟩ profile in figure 7(c). For the unladen flow, the sweep motion contributes more to turbulence production than ejection motions at $y^+ < 15$. Farther from the wall at $y^+ > 15$, the ejections become dominant as also observed in the DNS results of Kim et al. (1987). The beads with sweep and ejection motions also show a similar trend with the transition between sweep and ejection regions at $y^+ = 20$.

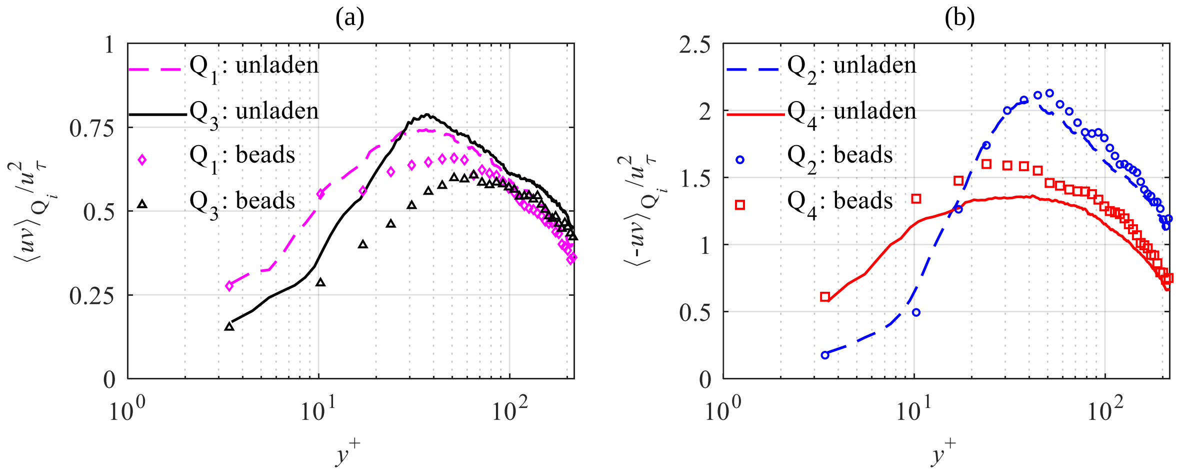

FIGURE 10. Conditional average of Reynolds shear stress of the unladen flow and beads based on motions in the (a) first and third, and (b) second and fourth u-v quadrants.

The quadrant analysis is extended in figure 11 to conditionally averaged acceleration, $A^+_{x,\mathrm{Q}i}$, of the unladen flow and beads to identify the contribution of quadrant motions to A_x^+. The beads with $v > 0$ (Q_1 and Q_2) gain momentum from the high-speed region by moving away from the wall and have $A_x^+ > 0$, except for Q_1 at $y^+ < 40$ where the viscous force are dominant. At $y^+ < 20$, only ejection motions of Q_2 result in positive A_x^+. The maximum of the conditionally averaged A_x^+ based on Q_2 for both the unladen flow and beads is almost at the outer boundary of the buffer layer, or y^+~30. At this location, the viscous effects diminish and the surrounding fluid accelerates the ejected fluid and beads. The larger wall-normal displacement of beads due to their inertia moves them further into the high-speed region. This results in higher drag force on the ejected beads compared with the ejected fluid. Therefore, the positive A_x^+ of beads is larger than that of the fluid, as shown in figure 11(b). It is also seen in this figure that in the near-wall region, sweep motions have $A_x^+ < 0$ for both the unladen flow and beads. The conditionally averaged A_x^+ based on Q_4 for unladen flow has a minimum at $y^+ \approx 8$ while the minimum for beads is found at $y^+ \approx 10$. The locations of the minimum values of these conditional averages are consistent with the locations of the minimum values of A_x^+ shown in figure 5(a) and figure 8(a), respectively. Comparison of figures 11(a) and (b) shows that for both the unladen flow and beads, ejections and sweeps (Q_2 and Q_4 quadrants) are the major turbulent motions which provide positive and negative A_x^+, respectively.

The conditionally averaged A_y^+ values, based again on u-v quadrant analysis, are shown in figure 12 for the unladen and bead-laden flows. As this figure shows, the positive A_y^+ of unladen flow is due to fluid elements with $v > 0$ (Q_1 and Q_2) in the whole near-wall region as well as sweep motions (Q_4) at $y^+ < 100$. The wall-normal pressure gradient induced by the low-pressure cores of the quasi-streamwise vortices pulls the flow upward and provides $A_y^+ > 0$. At $y^+ < 100$ for the unladen flow it is only the motions in Q_3 that have negative contribution to A_y^+. Similar trends are observed for beads but the values of A_y^+ are smaller because of gravity and their larger inertia compared with the unladen fluid flow. The Q_2 and Q_4 profiles for beads show that ejection and sweep motions have similar contribution to A_y^+ for the near-wall region: they both have $A_y^+ > 0$ at $y^+ < 40$ and $A_y^+ < 0$ at $y^+ > 40$. Figure 12 shows that for both unladen flow and beads, Q_1 and Q_3 have the major contributions to positive and negative A_y^+, respectively.

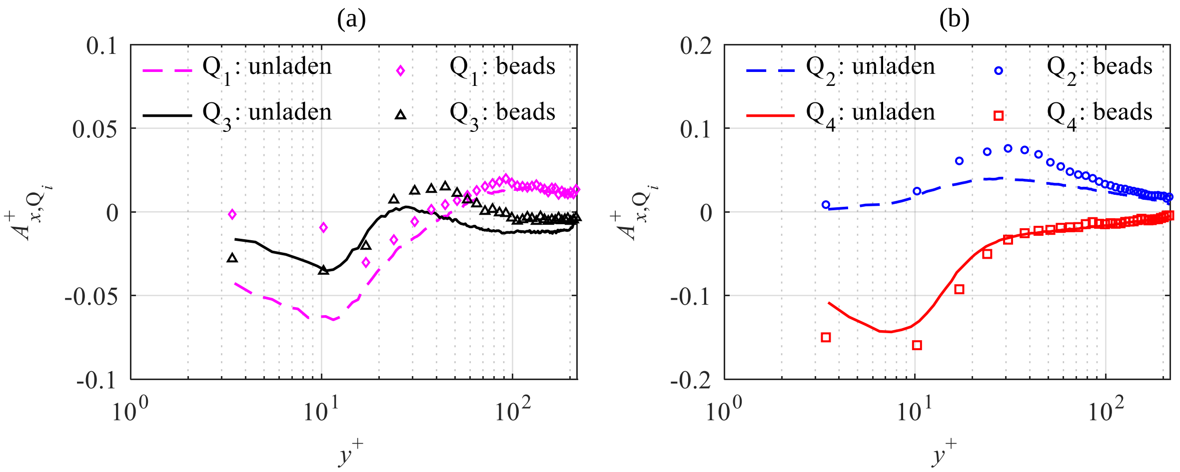

FIGURE 11. Conditional average of A_x^+ based on the motions in (a) first and third quadrants, and (b) second and fourth quadrants.

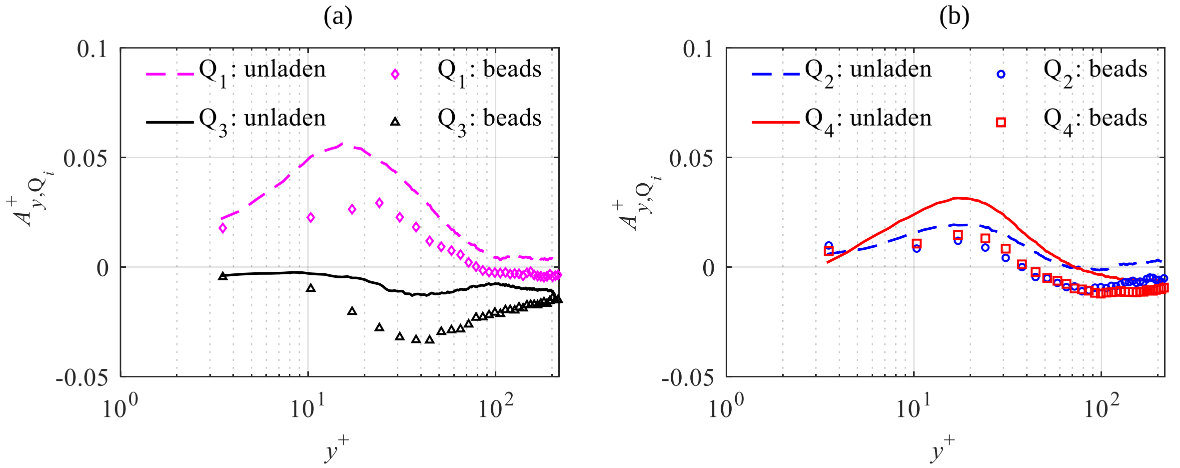

FIGURE 12. Conditional average of A_y^+ based on the motions in the (a) first and third quadrants, and (b) second and fourth quadrants.

6. Bead-wall interactions

In this section, the effect of the wall is analysed on beads with wall separation distance of $y_p < d_p$, where y_p is the distance between the bead center and the wall. The trajectory, velocity, and acceleration of these near-wall beads is investigated. In addition, the temporal scales of the near-wall trajectories and their collision with the wall is statistically characterized. The bead trajectories are analyzed based on the trajectory angle, θ, which is defined as $\tan^{-1}(V/U)$. Based on this definition and as seen in figure 13, a bead which is approaching the wall (i.e. $V < 0$) has a negative θ and a bead which is moving away from the wall (i.e. $V > 0$) has a positive θ. For a bead colliding with the lower wall of the channel, the impact angle, θ_i, and rebound angle, θ_r, are defined as the trajectory angle of the bead before and after collision, respectively. In total, more than 80,000 bead trajectories at $y_p < d_p$ were detected from 5 seconds of time-resolved 3D-PTV data.

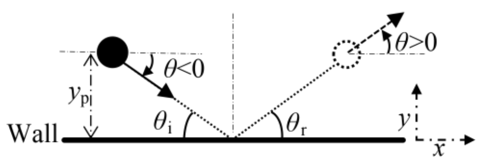

FIGURE 13. A schematic to define the parameters used to characterize bead collision with the lower wall of the channel.

6.1 *Trajectory angle*

To scrutinize the relation of θ with velocity fluctuations for the beads at $y_p < d_p$, the joint probability density function (jpdf) of θ and u/u_τ, and the jpdf of θ and v/u_τ is shown in figure 14(a) and (b), respectively. The jpdf has a drop-shaped contour with a large variation of θ for large negative u, and a small variation of θ for large positive u. Therefore, the smaller is the instantaneous streamwise velocity of the bead (U), the wider is the distribution of θ. This relation is pronounced here, since the mean streamwise velocity, $\langle U \rangle$, is small in the vicinity of the wall. The relation between θ and v is as expected; a positive v results in a positive θ, and vice versa. It is also observed that distribution of θ becomes wider with increasing v.

The pdf of θ for beads in the vicinity of the wall at $y_p < d_p$, i.e. y^+= 3.4, and higher y^+ locations are shown in figure 15. The pdf for y^+= 3.4 has a larger peak at $\theta = 0$, while the tails of the pdf extend to large positive and negative θ, reaching ±20°. This peaky behaviour of the pdf reduces with increasing y^+. At higher y^+, the peak of pdf attenuates and shift towards negative θ, which means that most of the trajectories descent toward the wall. It is also observed that the tail of the pdf disappears with increasing y^+ as the probability of large θ becomes negligible. Therefore, the larger θ events are limited to the vicinity of the wall where the instantaneous streamwise velocity of the beads is small.

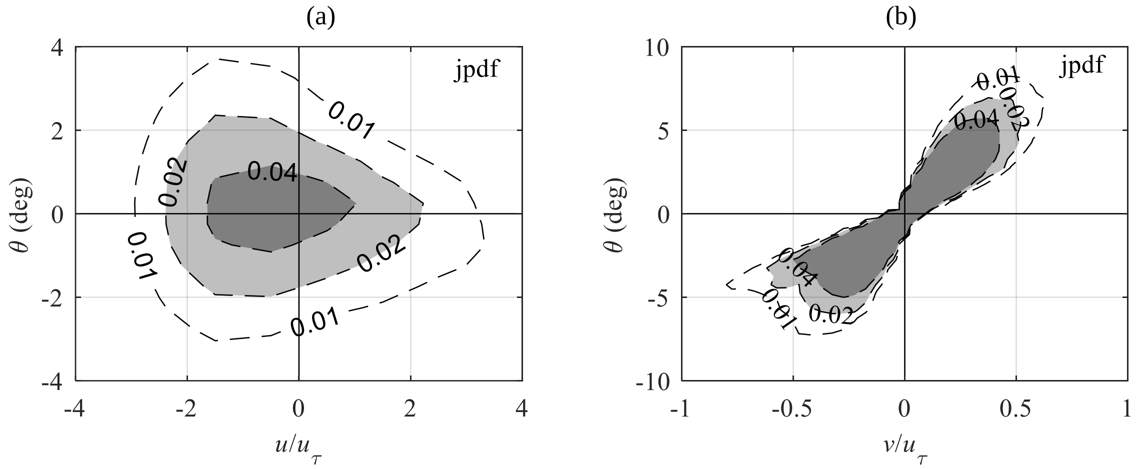

FIGURE 14. Joint probability density function of (a) u/u_τ and θ, and (b) v/u_τ and θ, for beads with $y_p < d_p$.

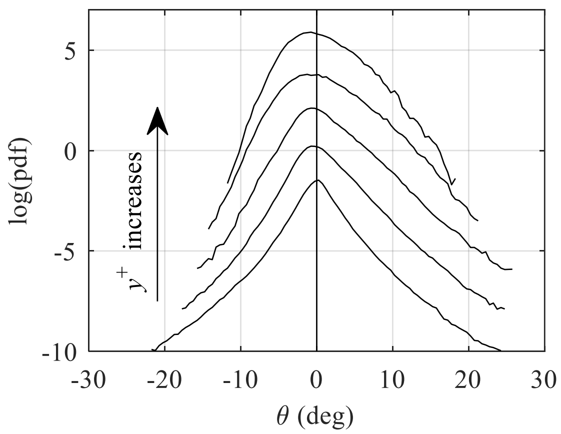

FIGURE 15. The pdf of θ for beads at y^+ = 3.4, 10.2, 17.0, 44.3, and 98.8, from bottom to top, respectively. The pdfs are shifted up by two units of the vertical axis for clarity.

6.2 *Velocity and acceleration*

Conditional averaging is applied here to investigate the contribution of each quadrant of velocity fluctuations to instantaneous velocity and acceleration of the near-wall beads, i.e. $y_p < d_p$. First, to characterize the distribution of the motions, jpdf of u and v fluctuations of the beads is presented in figure 16. The jpdf is relatively symmetric with respect to the horizontal axis (v = 0). Most of beads have u < 0 caused by (i) the fluid viscous force as the surrounding fluid has lower velocity than beads and (ii) bead-wall interactions. The contours are also slightly shifted toward v > 0 and more beads are in the second quadrant (Q_2) than the third quadrant (Q_3). Considering the smaller U of the fluid than the beads due to no-slip boundary condition at $y^+ = 3.4$, the Saffman force at this location should be downward. Therefore, it is the ejection motions, Magnus lift force, and wall collision, which can move the beads away from the wall and cause $v > 0$.

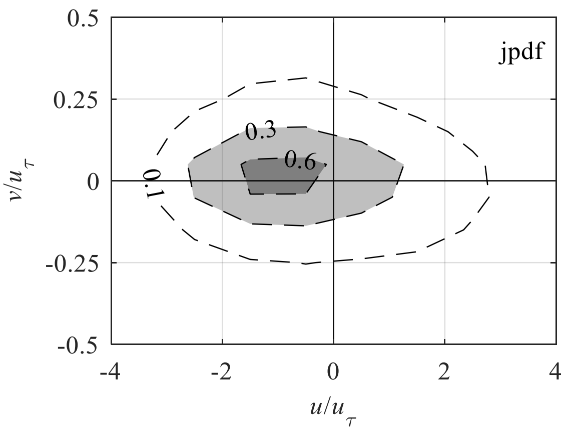

FIGURE 16. Joint probability density function of normalized velocity fluctuations. Only the beads with $y_p < d_p$ are considered.

The relation between instantaneous velocity and the absolute value of trajectory angle, $|\theta|$, is shown in figure 17(a) and (b) for the streamwise and wall-normal components, respectively. Results are also conditionally averaged based on the u-v quadrants of bead's motion. The conditional averaging is carried out for $|\theta| < 4^\circ$ with a bin size of 0.5°. The $|\theta| < 4^\circ$ range is applied to ensure statistical convergence as there are few beads outside of this range. As expected, the beads with Q_1 and Q_4 motion ($u > 0$) have larger U^+ than the beads with Q_2 and Q_3 motion ($u < 0$) in figure 17(a). The U^+ of the beads in the first quadrant (Q_1) is ~$6.3u_\tau$ and does not considerably change with $|\theta|$; streamwise velocity of the beads with Q_1 motion is not a function of the trajectory angle. For the beads with a sweep motion (Q_4), U^+ increases with increasing $|\theta|$ and reaches ~$7.5u_\tau$ at $|\theta| = 4^\circ$. This is because the beads with larger $|\theta|$ have come down from a higher y^+, and therefore have higher U^+. The U^+ value of the beads in Q_2 and Q_3 are almost equal at different $|\theta|$, and for both quadrants, U^+ slightly decreases with increasing $|\theta|$. As seen in figure 17(b), there is a linear relation between $|\theta|$ and V^+, which indicates that $|\theta|$ is mainly caused by variation of V and not U. The conditionally averaged values of V^+ also shows that the beads with Q_1 and Q_4 motions ($u > 0$) have a larger magnitudes of V^+ compared with the beads with Q_2 and Q_3 ($u < 0$). This means the faster beads (Q_1 and Q_4) have a larger wall-normal velocity, which diffuses their momentum in the wall-normal direction.

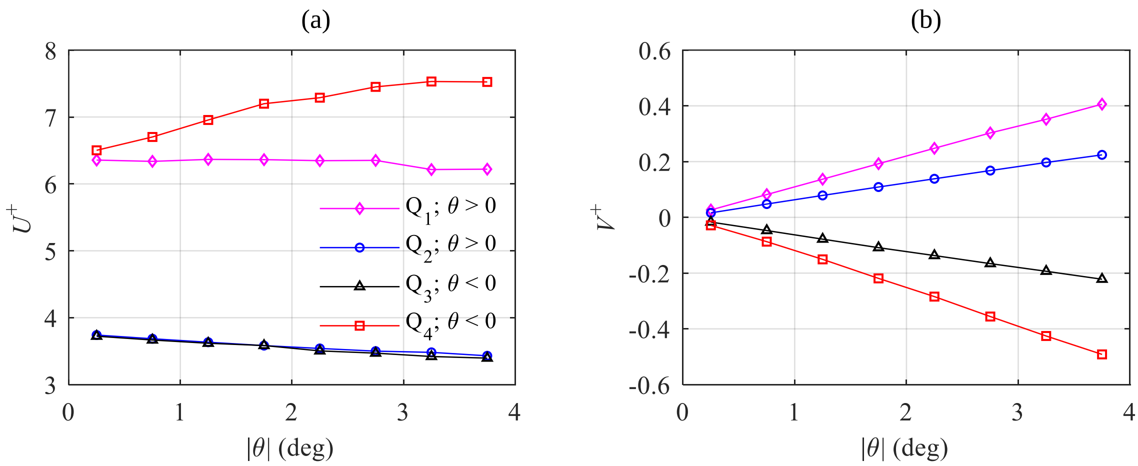

FIGURE 17. Conditionally averaged (a) U^+ and (b) V^+ of beads based on u-v quadrants as functions of $|\theta|$. Only the beads with $y_p < d_p$ are considered in this analysis.

The variation of conditionally averaged A_x^+ with $|\theta|$ is shown in figure 18(a) to compare the contributions of different quadrants. It is expected that the beads with upward motion (Q_1 and Q_2) accelerate in the streamwise direction as they move upward into the regions with higher U values. However, figure 18(a) shows that such a trend is only valid for $|\theta| > 1$, when the motion away from the wall is large enough. When the bead's ascent angle is smaller than 1°, A_x^+ for Q_1 and Q_2 motions is negative. The beads in Q_3 have downward motion ($\theta < 0$) and $A_x^+ < 0$. In all these cases, streamwise deceleration is associated with viscous deceleration by the near-wall fluid and particle-wall collisions. Figure 18(a) shows that beads with sweeping motion in Q_4 quadrant experience the highest streamwise deceleration. The deceleration of these beads also increases with increasing $|\theta|$. This larger deceleration of trajectories with large $|\theta|$ is associated with a larger viscous drag due to their greater velocity difference with respect to the surrounding fluid; the beads with larger $|\theta|$ have come down from higher y^+ locations with higher velocity.

The variation of conditionally averaged A_y^+ values is also investigated for the u-v quadrants and presented in figure 18(b). All four quadrants have a positive A_y^+. As it was explained previously, a positive A_y^+ indicates acceleration of upward moving beads and deceleration of downward moving beads. For sweeping motion of Q_4, a strong increase in A_y^+ with increasing $|\theta|$ is observed. The larger positive A_y^+ of the sweeping beads is attributed to greater wall-normal drag and wall repulsive force as they approach the wall under a larger $|\theta|$. A strong increase in A_y^+ with increasing $|\theta|$, is also observed for the upward moving beads ($v > 0$) in Q_1. Therefore, upward trajectories with a larger angle undergo a stronger wall-normal acceleration. A possible cause of this trend can be stronger ejection events which accelerate the beads upward under a larger ascent angle. The A_y^+ of beads with Q_2 motion slightly increases with increasing $|\theta|$, while A_y^+ of beads in Q_3 does not show a strong and monotonic dependence on $|\theta|$. In general, beads with $u > 0$ (Q_1 and Q_4) have greater A_y^+ than the beads with $u < 0$ (Q_2 and Q_3). As it was seen in figure 17(b), the beads with $u > 0$ have a larger V^+, which can cause a larger velocity difference relative to the surrounding fluid. Therefore, a larger drag force can act on beads with $u > 0$, which increases their A_y^+.

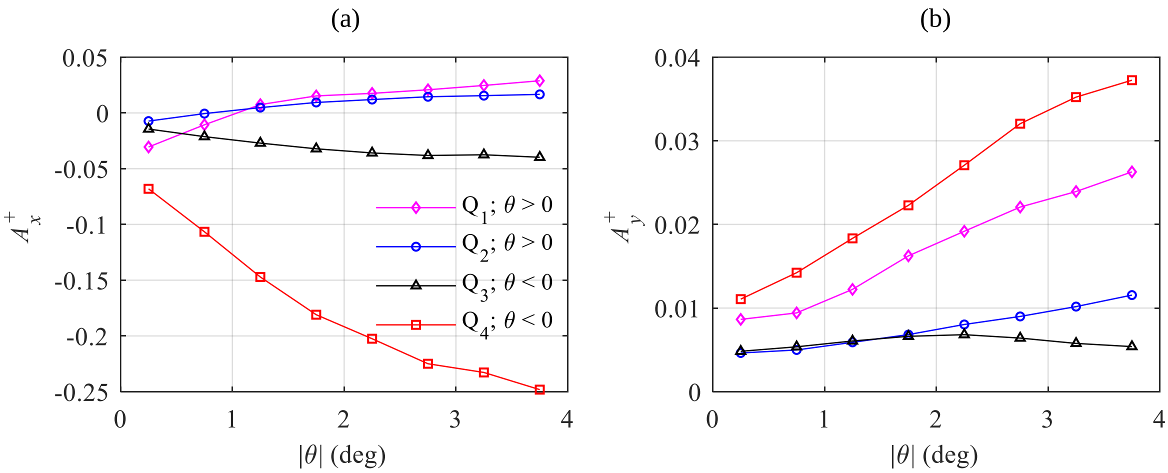

FIGURE 18. Conditionally averaged (a) A_x^+ and (b) A_y^+ of beads based on u-v quadrants as functions of $|\theta|$. Only the beads with $y_p < d_p$ are considered in this analysis.

6.3 *Temporal scales*

The temporal autocorrelation of beads' motion is investigated here to characterize their time-scales at different wall-normal distances. For a variable S, the autocorrelation coefficient is determined as $C_{SS}(t)=\langle S(t^+_0)\, S(t^+_0+t^+)\rangle/\langle S^2(t_0)\rangle$, where $S(t^+_0)$ is the value of S at the initial time step of t^+_0 and t^+ is the time shift. This autocorrelation is calculated from the time-resolved values of U, V, W, and θ along the bead trajectories. The results are shown in figure 19 at five different y^+. In general, all the autocorrelation coefficients decrease with increasing t^+. The C_{UU} coefficient indicates that streamwise velocity of the beads stays correlated for a longer time since C_{UU} stays positive for a long t^+, beyond the investigated range. However, C_{VV}, C_{WW}, and $C_{\theta\theta}$ coefficients reach close to zero within t^+<100 for all the investigated y^+.

The autocorrelation coefficients approach zero at a larger gradient with decreasing y^+, which indicates smaller time-scale of the beads motion. This is expected as the turbulent structures of fluid phase also become smaller with decreasing y^+. However, the C_{VV} and $C_{\theta\theta}$ at y^+ = 3.4 demonstrate a different trend due to the presence of local minimums and negative values. At y^+ = 3.4, with increasing t^+, there is an initial and rapid decrease of C_{VV} to a local minimum at t^+ = 11. This is followed by a small increase and then a reduction to negative values at t^+ = 20.

For the same wall-normal location of $y^+ = 3.4$, $C_{\theta\theta}$ rapidly decreases and reaches a local minimum also at $t^+ = 11$. The time shift, t^+, to reach negative C_{VV} and $C_{\theta\theta}$, both indicate the time-scale when the bead changes its wall-normal direction of motion, shift from upward to downward motion, and vice versa. However, the local minimum is more pronounced for $C_{\theta\theta}$ since θ is strongly modulated by the small magnitude of U according to $\theta = \tan^{-1}(V/U)$. Therefore, change in the direction of a weak wall-normal motion (small V) can result in a significant change of θ if U is small.

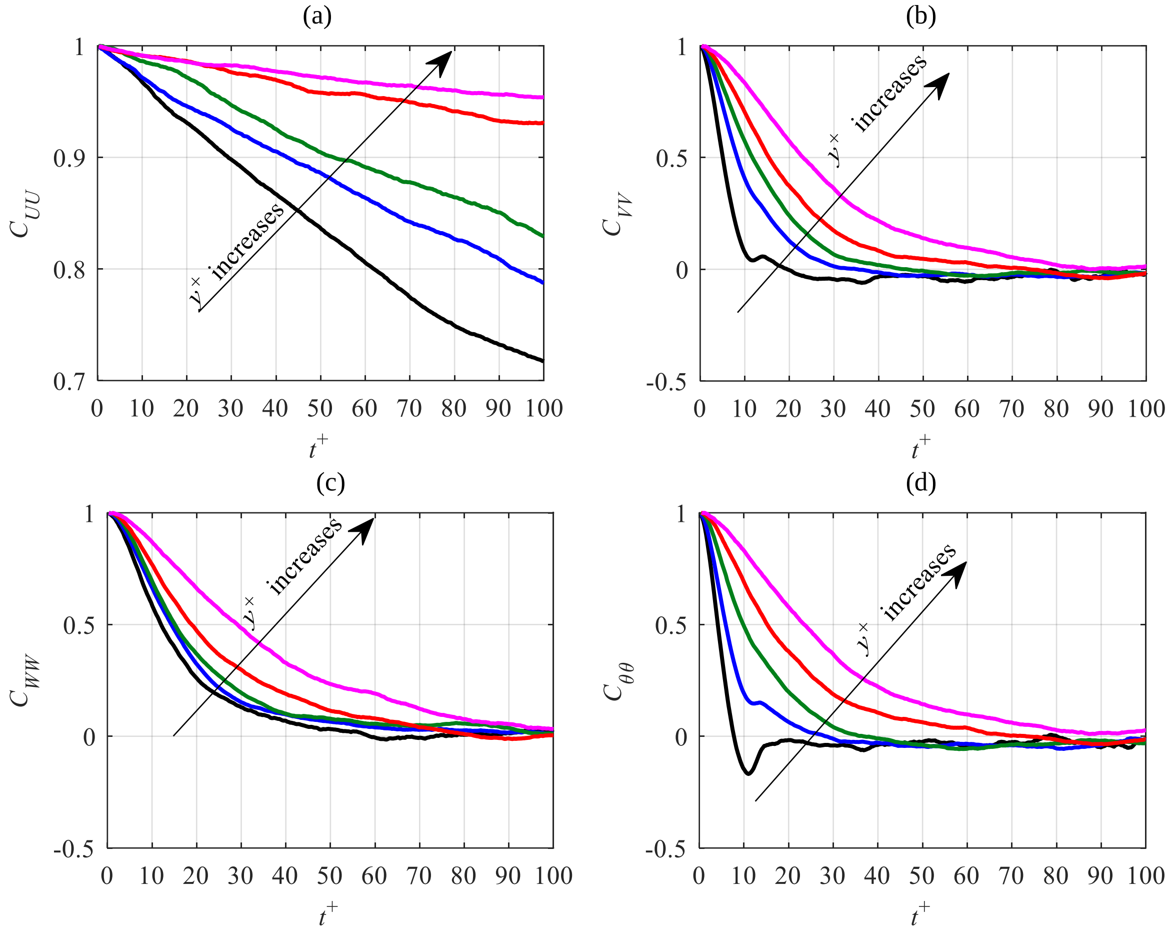

FIGURE 19. Temporal autocorrelation of (a) U, (b) V, (c) W, and (d) θ of glass beads. The curves in each plot, from bottom to top, correspond to $y^+ = 3.4$, 10.2, 17.0, 44.3, and 98.8.

6.4 *Collision with the wall*

The momentum exchange of beads during bead-wall collision is investigated by analysing bead trajectories that are in a narrower wall separation distance relative to the previous analysis. In this analysis, only beads that the distance of their centroid from the wall is equal to or smaller than the half of mean particle diameter (i.e. $y_p \leq 0.5d_p$) are considered. This resulted in about 34,000 bead trajectories within 5 seconds of time-resolved 3D-PTV data. For these near-wall trajectories, wall-collision is defined when the bead also has a negligible wall-normal velocity. This criterion is imposed when the instantaneous wall-normal bead velocity, V, is an order of magnitude smaller than the average of the absolute wall-normal bead velocity, $\langle|V|\rangle$. Therefore, $|V| < 0.1\langle|V|\rangle$, where $\langle|V|\rangle$ = 0.01 m/s at $y^+ = 3.4$. The period when this criterion is valid is defined as the wall-interaction time, t_i. For the tracks with a detected collision and within $y^+ \leq 0.5d_p^+$, the absolute value of trajectory angle before collision is averaged and indicated as $|\theta_i|$. The average trajectory angle after collision is also estimated and denoted as the average rebound angle, $\langle\theta_r\rangle$.

The variation of the estimated $\langle\theta_r\rangle$ with $|\theta_i|$ is presented in figure 20(a). For $|\theta_i| < 1.5°$, $\langle\theta_r\rangle$ is greater than $|\theta_i|$, meaning that trajectories with small θ rebound at a larger angle and disperse through collision with the wall. Beads with $|\theta_i| > 1.5°$ rebound at a smaller angle; $\langle\theta_r\rangle < |\theta_i|$. The normalized average of the wall-interaction time ($t_i^+ = \langle t_i\rangle/t_f$) is presented in figure 20(b) as a function of $|\theta_i|$. Inspection of the data shows that a bead with $|\theta_i| < 1.5°$ can spend on average $5t_f$ in contact with the wall. Such beads may have multiple small collisions with the wall or slide along it. The wall-interaction time scale approaches a constant value of about 1.6 for beads with $|\theta_i| > 1.5^o$.

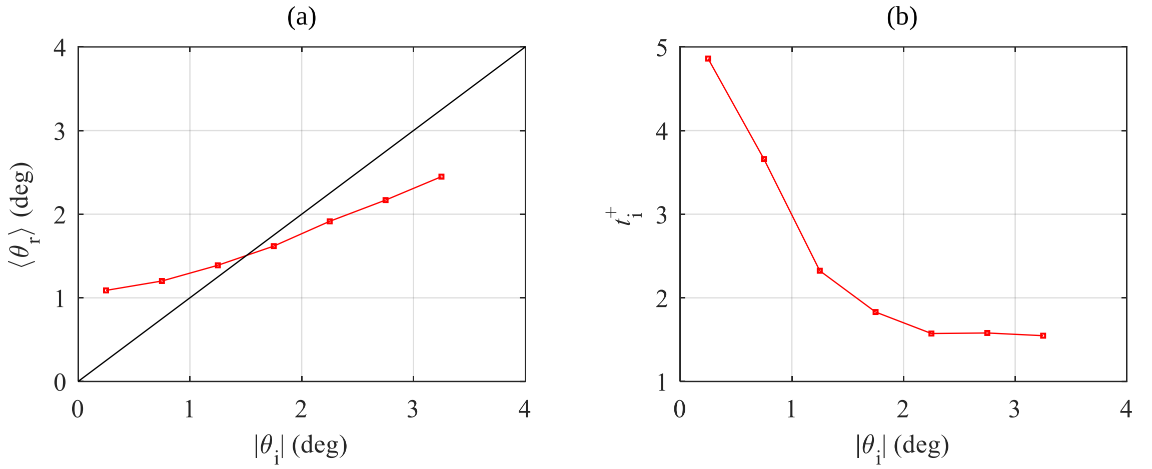

FIGURE 20. (a) The average rebound angle, and (b) the wall-interaction time scale of beads as a function of incident angle.

The average restitution ratio of beads (the ratio of the rebound velocity to the incident velocity) in streamwise direction, $\langle e_U\rangle$, and wall-normal, $\langle e_V\rangle$, are determined and presented in figure 21 to show their variation with $|\theta_i|$. Figure 21(a) shows that for small incident angles of $|\theta_i| < 1^o$, $\langle e_U\rangle$ is close to 1 which means that the sliding beads have negligible momentum exchange and undergo elastic collision in the streamwise direction. This is consistent with the smaller A_x^+ values observed for downward moving beads (Q_3 and Q_4) at small $|\theta|$, as seen in figure 18(a). As the incident angle becomes steeper ($|\theta_i| > 1^o$), $\langle e_U\rangle$ reduces to ~ 0.925 for $|\theta_i| > 2^o$. In other words, the streamwise momentum of these beads reduces by 7.5% due to collision with the wall.

The beads with $|\theta_i| < 1.5^o$ have wall-normal restitution ratios, $\langle e_V\rangle$, greater than 1 as seen in figure 21(b). These beads slide on the wall over a longer period of time as seen in figure 20(b). The longer interaction increases the angular velocity of a bead since the bottom surface of the bead is subject to surface friction due to the interaction with the wall, while its upper surface is subjected only to shear. This angular velocity is known to produce the Magnus lift force (Rubinow & Keller 1961). The Magnus force in the wall-normal direction can be determined as $F_{mag} = \pi d_p^3 \rho_f \omega (U_p - U_f)/8$ (Crow 2011). Here, ω is the angular velocity of a glass bead, which is approximated as the half of the local shear rate (Drew & Passman 1999). Based on the unladen mean velocity profile, the mean shear rate at $y^+ = 3.4$ is about 2800 1/s. At this wall-normal location, $\langle U_p\rangle$-$\langle U_f\rangle$ is about 0.09 m/s. Therefore, the approximate F_{mag} for a glass bead at $y^+ = 3.4$ is about 9.7×10^{-8} N. This force is about four times more than the weight of a glass bead (~2.5×10^{-8} N) and can potentially lift a glass bead. This type of particle motion, where particle lift occurs after some period of sliding on the bottom wall was observed in figure 3 and was also recently observed by Barros et al. (2018). Based on these observations, the fact that $\langle e_V\rangle > 1$ does not mean that the bead gains wall-normal momentum through collision with the wall; the excess momentum is due to the additional angular momentum which in turn produces a lift force. By increasing $|\theta_i|$, $\langle e_V\rangle$ decreases to a value of about 0.8 for the beads with $|\theta_i| > 1.75^o$. Generally, increasing the incident angle increases the wall-normal momentum loss and results in lower values of $\langle e_V\rangle$.

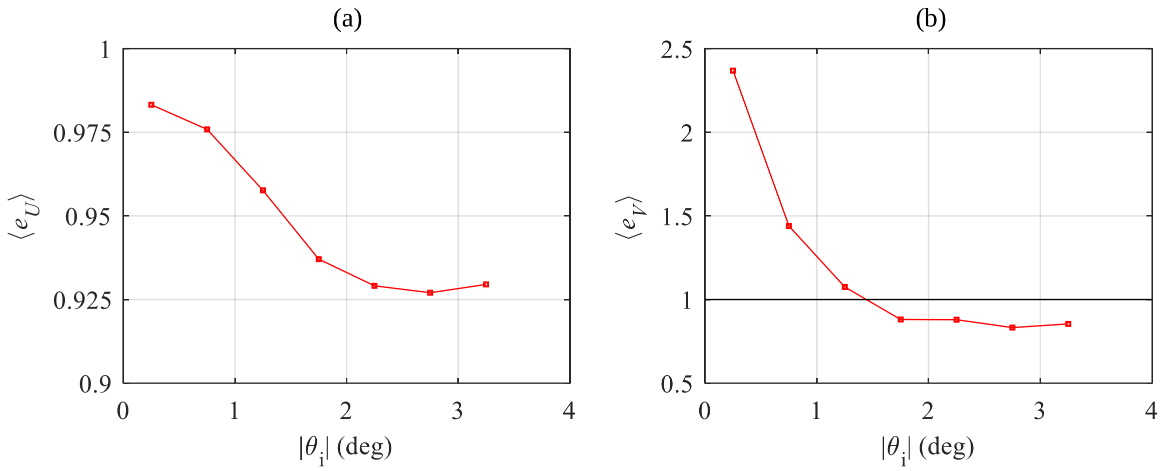

FIGURE 21. Variation of (a) streamwise and (b) wall-normal bead restitution ratios with absolute incident angle.

7. Summary and conclusions

To characterize acceleration statistics and wall-collision of inertial particles in non-isotropic near-wall turbulence, glass beads with d_p^+=6.8 at a volume concentration of 0.03% in a turbulent channel flow at Re_τ = 410 were investigated using time-resolved 3D-PTV. It has been shown that for glass beads, there are qualitative relations between the wall-normal variations of $\langle A_x\rangle$ and $\partial\langle uv\rangle/\partial y$ as well as $\langle A_y\rangle$ and $\partial\langle v^2\rangle/\partial y$. Comparison of the wall-normal acceleration of glass beads and unladen flow showed similarities between bead dynamics and the near-wall fluid dynamics. The investigations show presence of two layers based on the acceleration of the beads: (a) an inner layer in the vicinity of the wall at approximately y^+ < 20, and (b) an outer layer at farther distance from the wall at y^+ > 20.

Within the inner-layer, the beads decelerated (on average) in the streamwise direction. The maximum negative streamwise deceleration was observed at y^+ = 10 and it gradually reduced to zero at y^+ = 20. In the inner-layer, a large percentage of the beads had velocities less than the average bead velocity and their turbulent motions belonged to the second and the third quadrants of velocity fluctuations. However, the bead dynamics in this layer were dominated by the extreme motions of a smaller number of beads in the fourth quadrant. These beads had a sweeping motion toward the wall and demonstrated the largest streamwise momentum and deceleration. The wall-normal acceleration of the beads in the inner layer was positive, which indicated an increase in wall-normal velocity when a bead moves away from the wall, or a reduction of wall-normal velocity when a bead moves towards the wall.

In the outer layer, the beads had an overall positive streamwise acceleration, which peaked at approximately y^+=30. The peak was associated with the beads in the second quadrant, i.e. an ejection motion. The maximum transfer of momentum from the liquid phase to the beads occurred in the logarithmic layer, where the streamwise acceleration of the beads was large and positive. However, the streamwise acceleration gradually attenuated with increasing y^+. At farther distance from the wall, the positive streamwise acceleration of the beads moving away from the wall was balanced by the negative streamwise acceleration of the beads moving towards the wall. The outer-layer beads also had a negative wall-normal acceleration, which was associated with an increase in the wall-normal velocity of beads in the third and forth quadrant, and reduction in the wall-normal velocity of beads of the first and second quadrant.

The interaction of glass beads with the wall was studied by analysing the trajectory angle, velocity, and acceleration of the beads found in the immediate vicinity of the wall. At $y_p < d_p$, beads with sweeping motion had the maximum momentum, streamwise deceleration, and wall-normal acceleration compared with other beads. These terms increased with increasing the trajectory angle, $|\theta|$. At $y_p = d_p/2$, the bead trajectory angle had a peaky distribution; a large number of beads had a near zero angle while there were occasional extremely large trajectory angles of up to 20°. The latter was associated with the near-wall beads that had a small streamwise velocity. With increasing y^+, the trajectory angle did not demonstrate a peaky distribution, and the mode of the distribution was slightly negative as most of the beads gradually settled toward the wall. For beads within $y_p \leq d_p/2$, wall collision was defined when a bead had a negligible wall-normal velocity. The beads with an incident angle of $|\theta_i|$<1.5º had a longer average interaction time with the wall, which could be as long as ~5t_f. These beads were referred to as the sliding beads and had a negligible streamwise momentum exchange (~5%) during their interaction with the wall. It is conjectured that their longer interaction time increased the effect of Magnus lift force on them. As a result, their average rebound angle was larger than their incident angle and their wall-normal restitution coefficient was larger than one. The beads with sharper collision angle with the wall of $|\theta_i|$>1.5º had smaller streamwise and wall-normal restitution coefficients, and also a smaller average wall-interaction time. The autocorrelation coefficients of wall-normal velocity and trajectory angle had a local minimum with negative value at a time-shift of approximately 11t_f. This indicates the average time for change in the direction of wall-normal motions for the beads at $y_p \leq d_p/2$ due to their interaction with the wall. A negative autocorrelation coefficient was not observed for the beads at farther distance from the wall.

In general, this experimental investigation shows that the assumptions of point-particles and elastic particle-wall collision are inadequate for accurate modeling of large inertial beads in water. The discrepancy between the acceleration profiles from the experiments and those from the numerical simulation of Zamansky et al. (2011) showed that the point-particle assumption is not valid for larger particles (d^+_p=6.8) with small density relative to the carrier phase (ρ_p/ρ_f = 2.5). Measurements of particles velocity also showed evidence of prolonged interactions with the wall for particles that impact the wall at a shallow angle. This resulted in an increase of beads momentum, which cannot be accounted for using the steady-state drag of the point-particle model. In addition, the measurements demonstrated evidence of inelastic particle-wall collisions with considerable loss of momentum at larger impact angles.

Appendix A. Uncertainty evaluation

A quadratic regression is applied on each position component of the tracers and glass beads along their trajectory to reduce the noise and estimate their velocity and acceleration. A quadratic regression over a long period (i.e. large temporal kernel) can filter out the high-frequency content of the data while a short kernel may not be effective in reducing the noise. Therefore, the size of the temporal kernel of the quadratic fit is optimized by evaluating the minimum kernel length just before the increase in noise of acceleration rms following the method used by Gerashchenko et al. (2008). The variation of the normalized rms of streamwise acceleration, $a_x^+ = a_x/(u_\tau^3/\upsilon)$, of tracers with the temporal kernel size is evaluated in figure A1 at y^+ = 3.4. It is observed that a_x^+ rapidly increases when the kernel size becomes smaller than 3 ms. The point where the variation of a_x^+ with reduction of the kernel size deviates from a straight line (more than 1%) is selected as the appropriate temporal kernel size. This optimum kernel is estimated at t = 4.5 ms in figure A1.

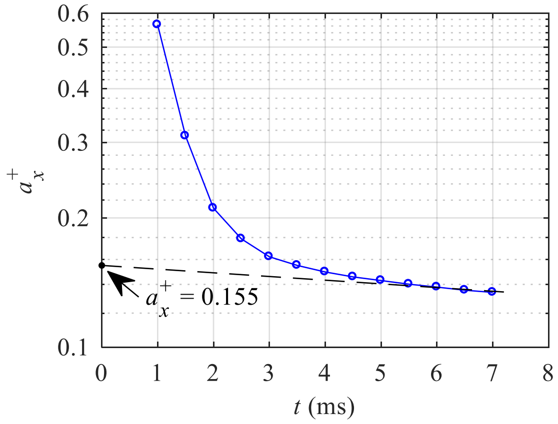

FIGURE A1. The dependence of streamwise acceleration rms of the tracers at y^+ = 3.4 on the temporal kernel of the quadratic regression fit. The dashed straight line shows the fitted line based on the method presented by Voth et al. (2002). The extrapolation of a_x^+ to t = 0 based on this fit is 0.155.

Voth et al. (2002) showed that the acceleration rms can be estimated as a summation of an exponential term (represents the contribution of turbulence) and a power law term (represents the contribution of position noise). They argued that an estimation of the acceleration rms can be obtained by extrapolation of the exponential term to zero temporal kernel. They confirmed that this extrapolation overestimates the true value of acceleration variance by about 10% based on comparison with the DNS results of Vedula & Yeung (1999). The extrapolation of the exponential term to t = 0 in figure A1 results in a_x^+= 0.155 which is about 13% larger than the a_x^+= 0.137 at y^+ = 3.4 obtained based on a kernel of 4.5 ms.

The performance of the quadratic regression in reducing the noise in estimating particle position is investigated by calculating the pre-multiplied linear spectral density (LSD) of the x, y, and z components of tracer trajectories before and after applying the polynomial regression, following the method of Gesemann et al. (2016). The result is presented in figure A2 as a function of the frequency, f, normalized by the Nyquist frequency, f_N, for positional error in x, y, and z location of tracers. When no polynomial regression is applied, a flat section is observed in the high-frequency end of the LSD, which shows the measurement noise. Based on this flat section, the estimated noise level is about 6, 10, and 5 µm that is equivalent to 0.1, 0.2, and 0.1 pixel in x, y, and z directions, respectively. As expected, the out of plane component has a larger noise level. As seen in figure A2, the quadratic regression reduced the high-frequency random noise while it does not affect the low-frequency motions. The normalized cross-over frequency, frequency at which the LSD profile after regression crosses the estimated noise level, is 0.49, 0.18, and 0.51 for the x, y, and z components, respectively.

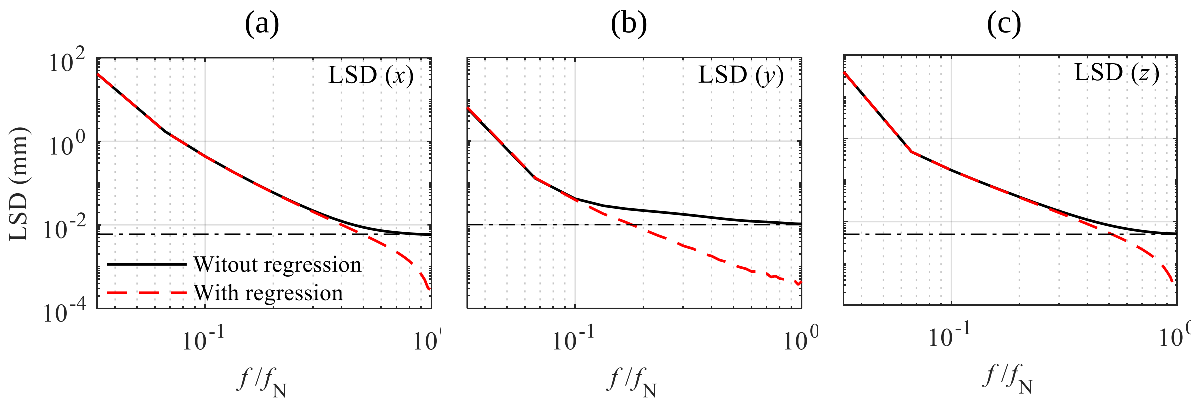

Figure A2: Linear spectral density of (a) x-, (b) y-, and (c) z-components of tracers' position in unladen flow with and without applying quadratic regression. The dashed-dotted lines show the measurement noise level in each component.

The difference between the measured velocity statistics of the unladen flow at y^+ = 3.4 with those from DNS of Moser et al. (1999) at Re_τ = 395 is presented in table A1. For acceleration statistics, the measured statistics of the unladen flow are compared with DNS of Yeo et al. (2010) at Re_τ = 410. It should be noted that the difference between the velocity statistics of the present study and the DNS of Moser et al. (1999) can be partially due to the small difference in Re_τ.

$\langle U\rangle$ m/s	$\langle u^2\rangle$ (m/s)^2	$\langle v^2\rangle$ (m/s)^2	$\langle w^2\rangle$ (m/s)^2	$\langle uv\rangle$ (m/s)^2	$\langle A_x\rangle$ m/s^2	$\langle A_y\rangle$ m/s^2	a_x m/s^2	a_y m/s^2
6×10^{-3}	3×10^{-3}	4×10^{-4}	2×10^{-4}	5×10^{-4}	0.8	0.4	2.2	8.9

TABLE A1. An estimation of uncertainty of 3D-PTV measurements based on the difference between the measured velocity and acceleration statistics in unladen flow with those of DNS at y^+ = 3.4. The DNS of Moser et al. (1999) at Re_τ=395 is used for velocity statistics, and DNS of Yeo et al. (2010) at Re_τ=410 is used for acceleration statistics.

Appendix B. Statistical convergence

The expected value of a discrete random variable, S, with finite outcomes s_n, is defined as $\mathrm{E}(S) = \sum_{n=1}^{N} s_n P(s_n)$, where $P(s_n)$ is the probability, and N is the total number of data points (Montgomery and Runger 2002). The ensemble average of S, denoted by $\langle S \rangle$, is equal to $\mathrm{E}(S)$ when N approaches infinity. The convergence of the velocity and acceleration statistics of unladen and particle-laden flows is investigated at different y^+ by determining the ratio of $\langle S \rangle/\mathrm{E}(S)$ for each variable, as shown in figure B1. This ratio is close to one for velocity and acceleration statistics in the whole measurement domain for unladen and particle-laden flows, showing the convergence of the investigated statistics. The maximum deviation from one among all the variables is for $\langle A_z \rangle/\mathrm{E}(A_z)$ of unladen flow at $y^+ = 170$ that is about 3%.

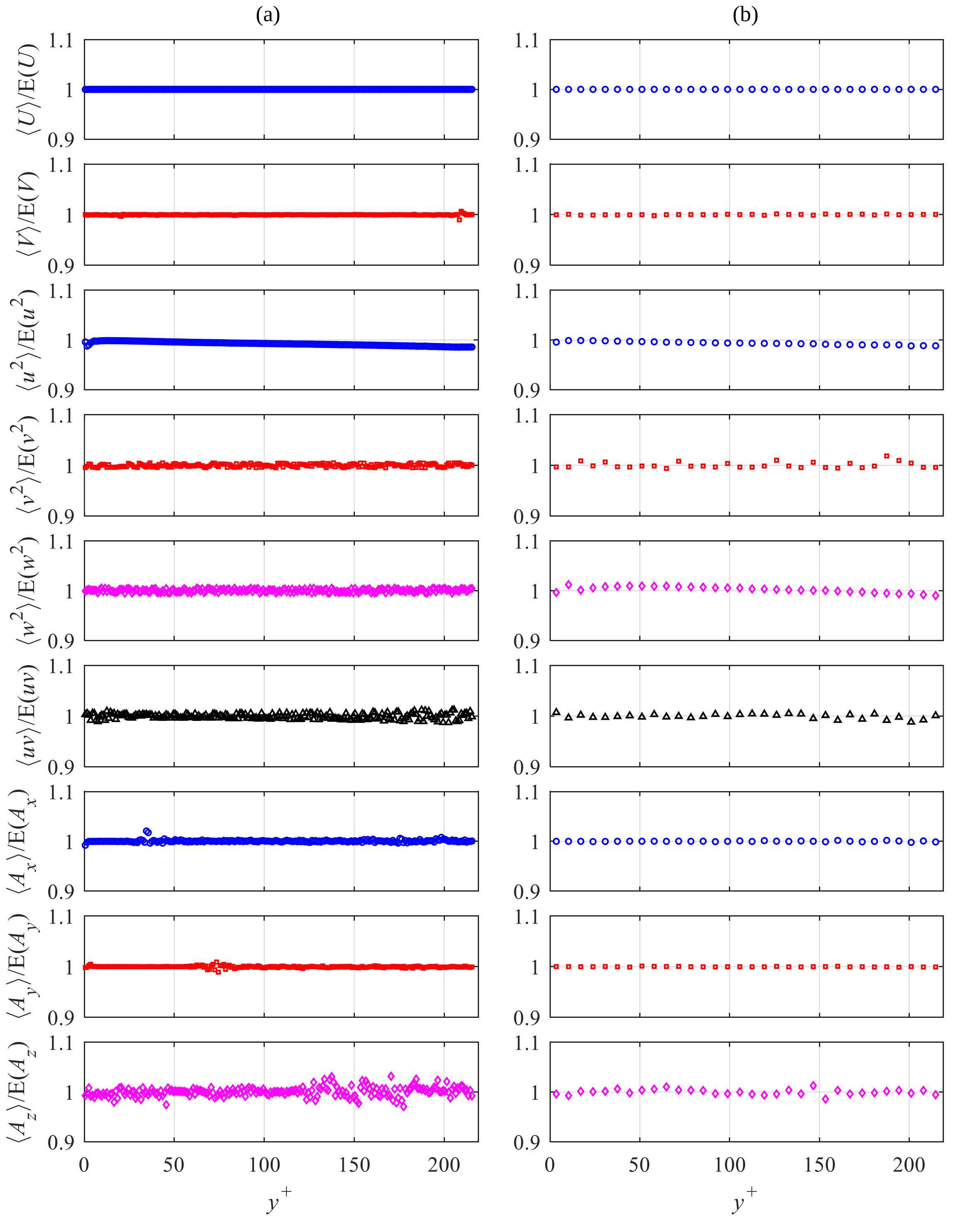

FIGURE B1. The ratio of the ensemble average of velocity and acceleration statistics over their associated expected value for (a) unladen flow, and (b) beads in particle-laden flow.

The convergence of first and second-order statistics of velocity and acceleration of glass beads is also investigated at $y^+ = 16.7$, as shown in figure B2. The selected location coincides with peak location of $\langle u^2 \rangle$. The random error of the velocity and acceleration statistics is calculated as the standard deviation of the last 20% of data (from n/N of 0.8 to 1) and was presented in table 4 of §2.

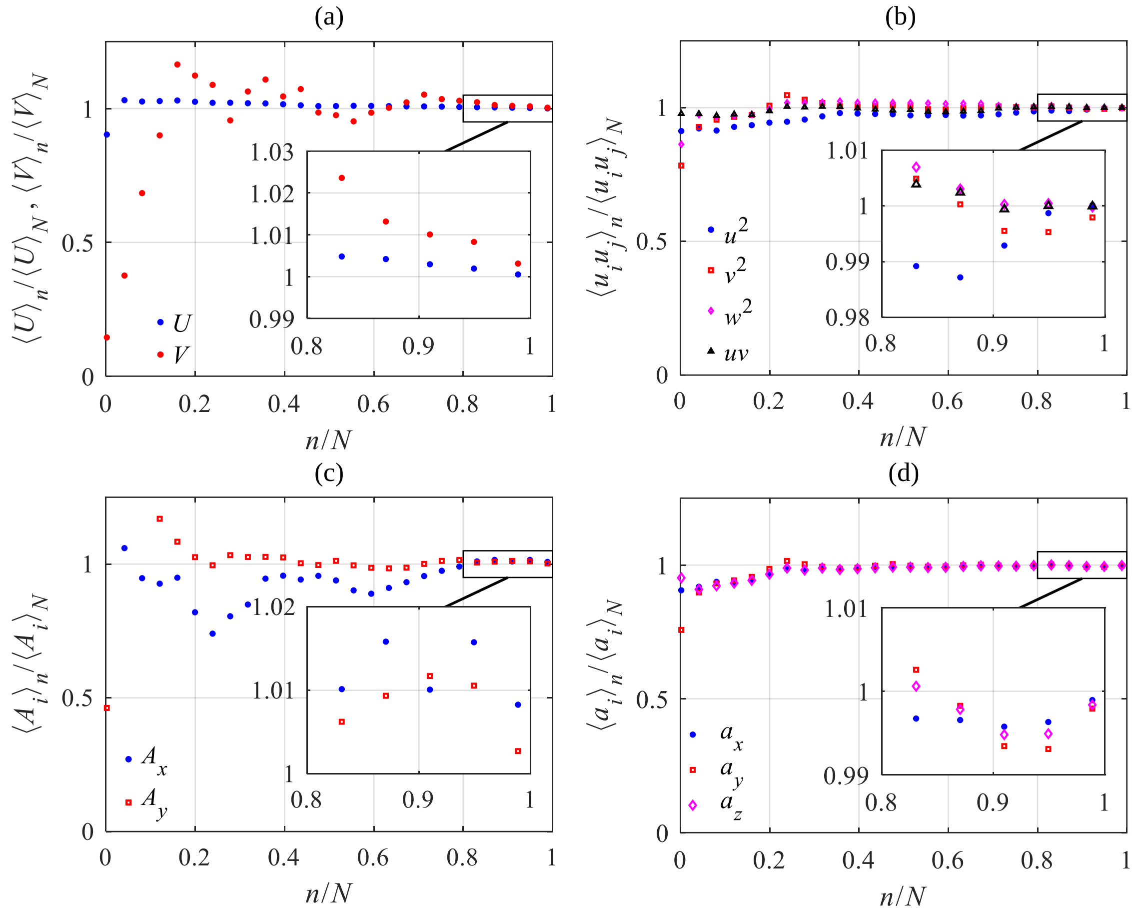

FIGURE B2. Variations of ensemble averaged values of (a) mean streamwise velocity (b) Reynolds stresses, (c) average acceleration, and (d) rms of acceleration of glass beads at $y^+ = 16.7$. The total number of data points is $N = 2.82 \times 10^6$.

REFERENCES

AHMADI, F., EBRAHIMIAN, M., SANDERS, R.S. and GHAEMI, S., 2019 Particle image and tracking velocimetry of solid-liquid turbulence in a horizontal channel flow. *Int J Multiphase Flow*, **112**, pp.83-99.

ALISEDA, A., CARTELLIER, A., HAINAUX, F. & LASHERAS, J. C. 2002 Effect of preferential concentration on the settling velocity of heavy particles in homogeneous isotropic turbulence. *J. Fluid Mech.* **468**, 77-105.

AYYALASOMAYAJULA, S., GYLFASON, A., COLLINS, L. R., BODENSCHATZ, E. & WARHAFT, Z. 2006 Lagrangian measurements of inertial particle accelerations in grid generated wind tunnel turbulence. *Phys. Rev. Lett*, **97**, 144507.

BARROS, D., HILTBRAND, B. &; LONGMIRE, E. K. 2018 Measurement of the translation and rotation of a sphere in fluid flow. *Exp. in Fluids* **59** (6), 14.

BEC, J., BIFERALE, L., BOFFETTA, G., CELANI, A., CENCINI, M., LANOTTE, A., MUSACCHIO, S. & TOSCHI, F. 2006 Acceleration statistics of heavy particles in turbulence. *J. Fluid Mech*. **550**, 349-358.

BRENNER, H., 1961 The slow motion of a sphere through a viscous fluid towards a plane surface. *Chem. Eng. Science* **16** (3-4), 242-251.

CALZAVARINI, E., VOLK, R., LÉVÊQUE, E., PINTON, J.F. & TOSCHI, F., 2012 Impact of trailing wake drag on the statistical properties and dynamics of finite-sized particle in turbulence. *Phys. D: Nonlin. Phenom.* **241**, 237-244.

CHEN, L., COLEMAN, S. W., VASSILICOS, J. C. & HU, Z. 2010 Acceleration in turbulent channel flow. *J. Turbulence*, **11**, N41.

CROWE, C., SCHWARZKOPF, J., SOMMERFELD, M. & TSUJI, Y. 2012 *Multiphase Flows with Droplets and Particles*. Boca Raton: CRC Press.

DREW, D. A. & PASSMAN S. 1999 *Theory of Multicomponent Fluids*, Springer.

EATON, J.K. & FESSLER, J.R., 1994 Preferential concentration of particles by turbulence. *Int. J. Multiphase Flow* **20**, 169-209.

ELGHOBASHI, S. 1994 On predicting particle-laden turbulent flows. *Applied Scientific Research* **52**, 309-329.

ELSINGA, G.E., SCARANO, F., WIENEKE, B. and VAN OUDHEUSDEN, B.W., 2006 Tomographic particle image velocimetry. *Exp Fluids*, **41**(6), pp.933-947.

FENG, J., HU, H. H. & JOSEPH, D. D. 1994 Direct simulation of initial value problems for the motion of solid bodies in a Newtonian fluid. Part 2. Couette and Poiseuille flows. *J. Fluid Mech.* **277**, 271-301.

GERASHCHENKO, S., SHARP, N. S., NEUSCAMMAN, S. & WARHAFT, Z. 2008 Lagrangian measurements of inertial particle accelerations in a turbulent boundary layer. *J. Fluid Mech*. **617**, 255-281.

GESEMANN, S., HUHN, F., SCHANZ, D. & SCHRÖDER, A. 2016 From noisy particle tracks to velocity, acceleration and pressure fields using B-splines and penalties. In *18th International Symposium on the Applications of Laser and Imaging Techniques to Fluid Mechanics (Lisbon, Portugal, 4–7 July)*.

GHAEMI, S. & SCARANO 2010 Multi-pass light amplification for tomographic particle image velocimetry applications. *Meas. Sci. Technol*. **21(12)**, 127002.

GONDRET, P., LANCE, M. & PETIT, L. 2002 Bouncing motion of spherical particles in fluids. *Phys. Fluids* **14**, 643–652.

HETSRONI, G., 1989 Particles-turbulence interaction. *Int J Multiphase Flow,* **15**(5), pp.735-746.

JOSEPH, G.G. & HUNT, M.L., 2004 Oblique particle-wall collisions in a liquid. *J. Fluid Mech*. 510, 71-93.

JOSEPH, G. G., ZENIT, J. R., HUNT, M. L. & ROSENWINKEL, A. M. 2001 Particle-wall collision in a viscous fluid. *J. Fluid Mech*. **433**, 329–346.

KAFTORI, D., HETSRONI, G. & BANERJEE, S. 1995a Particle behavior in the turbulent boundary layer. I. Motion, deposition, and entrainment. *Phys. Fluids* **7**,1095-1106.

KAFTORI, D., HETSRONI, G. & BANERJEE, S. 1995b Particle behavior in the turbulent boundary layer. II. Velocity and distribution profiles. *Phys. Fluids* **7**, 1107-1121.

KIGER, K. T. & PAN, C., 2002 Suspension and turbulence modification effects of solid particulates on a horizontal turbulent channel flow. *J. Turbulence* **3**, 1-17.

KIM, J., & BALACHANDAR, S., 2012 Mean and fluctuating components of drag and lift forces on an isolated finite-sized particle in turbulence. *Theoret. Comput. Fluid Dynam.* **26**, 185-204.

KIM, I., ELGHOBASHI, E. & SIRIGNANO, W. A. 1998 On the equation for spherical-particle motion: effect of Reynolds and acceleration numbers. *J. Fluid Mech.* **267**, 221–253.

KIM, J., MOIN, P. & MOSER, R. 1987 Turbulence statistics in fully developed channel flow at low Reynolds number. *J. Fluid Mech*. **177**, 133–166.

KIM, J. 1989 On the structure of pressure fluctuations in simulated turbulent channel flow. *J. Fluid Mech.*, **205**, 421-451.

KOSINSKI, P. & HOFFMANN, A.C., 2009 Extension of the hard-sphere particle-wall collision model to account for particle deposition. *Physical review E,* **79** (6), 061302.

KULICK, J.D., FESSLER, J.R. & EATON, J.K., 1994 Particle response and turbulence modification in fully developed channel flow. *J Fluid Mech*, **277**, pp.109-134.

KUSSIN, J. & SOMMERFELD, M. 2002 Experimental studies on particle behaviour and turbulence modification in horizontal channel flow with different wall roughness. *Exp. in Fluids* **33**, 143-159.

LAVEZZO, V., SOLDATI, A., GERASHCHENKO, S., WARHAFT, Z. & COLLINS, L. R. 2010 On the role of gravity and shear on inertial particle accelerations in near-wall turbulence. *J. Fluid Mech*. **658**, 229-246.

LEE, S. & LEE, C. 2005 Intermittency of acceleration in isotropic turbulence. *Phys. Rev. E* **71**, 056310.

LEE, C., YEO, K. & CHOI, J. I. 2004 Intermittent nature of acceleration in near wall turbulence. *Phys. Rev. lett.* **92**, 144502.

LEGENDRE, D., ZENIT, R., DANIEL, C. & GUIRAUD, P., 2006 A note on the modelling of the bouncing of spherical drops or solid spheres on a wall in viscous fluid. *Chem. Eng. Science*, **61** (11), 3543-3549.

LUO, K., HU, C., WU, F. & FAN, J., 2017 Direct numerical simulation of turbulent boundary layer with fully resolved particles at low volume fraction. *Phys Fluids*, **29**(5), p.053301.

MARCHIOLI, C. & SOLDATI, A. 2002 Mechanisms for particle transfer and segregation in a turbulent boundary layer. *J. Fluid Mech.* **468**, 283-315.

MAXEY, M. R. & RILEY, J. J. 1983 Equation of motion for a small rigid sphere in a non-uniform flow. Phys. Fluids **26** (4), 883-889.

MEI, R. W. & ADRIAN, R. J. 1992 Flow past a sphere with an oscillation in the free stream velocity and unsteady drag at finite Reynolds number. *J. Fluid Mech*. **237**, 323-341.

MELLER, Y. & LIBERZON, A. 2015 Particle-fluid interaction forces as the source of acceleration PDF invariance in particle size. *Int. J. of Multiphase Flow*, **76**, 22-31.

MILOJEVIÉ, D., 1990 Lagrangian stochastic-deterministic (LSD) predictions of particle dispersion in turbulence. Part. *Part. Syst. Charact*. **7**, 181–190.

MONTGOMERY, D.C. & RUNGER G.C. 2002 *Applied Statistics and Probability for Engineers, 3rd Edition*, Wiley.

MOSER, R. D., KIM, J. & MANSOUR, N.N. 1999 Direct numerical simulation of turbulent channel flow up to Re_τ=590. *Phys. Fluids* **11**, 943-945.

NASR, H. and AHMADI, G., 2007 The effect of two-way coupling and inter-particle collisions on turbulence modulation in a vertical channel flow. *Int J Heat and Fluid Flow*, **28**(6), pp.1507-1517.

NINO, Y. & GARCIA, M. H. 1996 Experiments on particle-turbulence interactions in the near–wall region of an open channel flow: implications for sediment transport. *J. Fluid Mech*. **326**, 285–319.

PRANDTL, L 1932 Recent results of turbulence research. Technical Memorandum 720, National Advisory Committee for Aeronautics.

RUBINOW, S.I. & KELLER, J.B., 1961 The transverse force on spinning sphere moving in a viscous fluid, *J. Fluid Mech.*, **11**, 447.

SALMAN, A.D., VERBA, A., LUKENICS, Z. & SZABO, M., 1989 Effects of Impact Velocity and Angle on Collision and Particle Velocity after Collision. *Periodica Polytechnica, Budapest*, 31.

SCHANZ, D., GESEMANN, S. & SCHRÖDER, A. 2016 Shake-The-Box: Lagrangian particle tracking at high particle image densities. *Exp. in Fluids* **57**, 1–27.

SCHRÖDER, A., SCHANZ, D., MICHAELIS, D., CIERPKA, C., SCHARNOWSKI, S. & KÄHLER, C. J. 2015 Advances of PIV and 4D-PTV "Shake-The-Box" for Turbulent Flow Analysis–the Flow over Periodic Hills. *Flow, Turbulence and Combustion*, **95**,193-209.

SHAO, X., WU, T. & YU, Z. 2012 Fully resolved numerical simulation of particle-laden turbulent flow in a horizontal channel at a low Reynolds number. *J. Fluid Mech*. **693**, 319-344.

SHOKRI, R., GHAEMI, S., NOBES, D. S. & SANDERS, R.S. 2017 Investigation of particle-laden turbulent pipe flow at high-Reynolds-number using particle image/tracking velocimetry (PIV/PTV). *Int. J. Multiphase Flow*, **89**, 136-149.

SOLDATI, A. 2005 Particles turbulence interactions in boundary layers. *ZAMM-Journal of Applied Mathematics and Mechanics/Zeitschrift für Angewandte Mathematik und Mechanik*, **85**, 683-699.

SOMMERFELD, M. & HUBER, N. 1999 Experimental analysis and modelling of particle-wall collisions. *Int J. of Multiphase Flow* **25**, 1457–1489.

SOMMERFELD, M. & LAIN, S., 2018 Stochastic modelling for capturing the behaviour of irregular-shaped non-spherical particles in confined turbulent flows. *Powder Technology* **332**, 253-264.

STELZENMULLER, N., POLANCO, J.I., VIGNAL, L., VINKOVIC, I. and MORDANT, N., 2017 Lagrangian acceleration statistics in a turbulent channel flow. *Phys Rev Fluids*, **2**(5), p.054602.

STOCCHINO, A. AND GUALA, M., 2005 Particle-wall collision in shear thinning fluids. *Exp. in Fluids*, **38** (4), pp.476-484.

TOSCHI, F. & BODENSCHATZ, E. 2009 Lagrangian Properties of Particles in Turbulence. *Annual Review of Fluid Mechanics*, **41**, 375-404.

TSUJI, Y., MORIKAWA, Y., TANAKA, T., NAKATSUKASA, N. & NAKATANI, M., 1987 Numerical simulation of gas-solid two-phase flow in a two-dimensional horizontal channel. *Int. J. Multiphase Flow*, **13** (5), 671-684.

VEDULA, P. & YEUNG, P. K. 1999 Similarity scaling of acceleration and pressure statistics in numerical simulations of isotropic turbulence. *Phys. Fluids* **11**, 1208–1220.

VOTH, G.A., LA PORTA, A., CRAWFORD, A. M., ALEXANDER, J. & BODENSCHATZ, E. 2002 Measurement of particle accelerations in fully developed turbulence. *J. Fluid Mech*. **469**, 121–160.

WALLACE, J. M., ECKELMANN, H. & BRODKEY, R. S. 1972 The wall region in turbulent shear flow. *J. Fluid Mech.* **54**, 39–48.

WIENEKE, B. 2008 Volume self-calibration for 3D particle image velocimetry. *Exp. in Fluids* **45**, 549-556.

WIENEKE, B. 2013 Iterative reconstruction of volumetric particle distribution. *Measurement Science and Technology* **24** 024008.

YEO, K., KIM, B.G. & LEE, C. 2010 On the near-wall characteristics of acceleration in turbulence. *J. Fluid Mech.* **659**, 405–419.

YEUNG, P. K. & POPE, S. B. 1989 Lagrangian statistics from direct numerical simulations of isotropic turbulence. *J. Fluid Mech*. **207**, 531–586.

YU, W., VINKOVIC, I. & BUFFAT, M. 2016 Acceleration Statistics of Finite-Size Particles in Turbulent Channel Flow in the Absence of Gravity. *Flow, Turbulence and Combustion* **96**, 183–205.

YU, Z., LIN, Z., SHAO, X. & WANG, L.P., 2017 Effects of particle-fluid density ratio on the interactions between the turbulent channel flow and finite-size particles. *Phys Rev E*, **96**(3), p.033102.

ZAMANSKY, R., VINKOVIC, I. & GOROKHOVSKI, M. 2011 Acceleration statistics of solid particles in turbulent channel flow. *Phys. Fluids* **23**, 113304.